

# The LC3B FRET biosensor monitors the modes of action of ATG4B during autophagy in living cells

Elif Begüm Gökerküçük<sup>1</sup>, Angélique Cheron<sup>1</sup>, Marc Tramier<sup>1,\*</sup>, Giulia Bertolin<sup>1,2,\*</sup>.

<sup>1</sup> Univ Rennes, CNRS, IGDR (Institute of Genetics and Development of Rennes), UMR 6290, F-35000 Rennes, France

<sup>2</sup> Lead contact

\* Correspondence and requests for materials should be addressed to G.B. ([giulia.bertolin@univ-rennes1.fr](mailto:giulia.bertolin@univ-rennes1.fr); Tel: +330223237516) or to M.T. ([marc.tramier@univ-rennes1.fr](mailto:marc.tramier@univ-rennes1.fr); Tel: +330223235487).

## **Abstract**

Although several mechanisms of autophagy have been dissected in the last decade, following this pathway in real time remains challenging. Among the early events leading to autophagy activation, the ATG4B protease primes the key autophagy player LC3B. Given the lack of reporters to follow this event in living cells, we developed a Förster's Resonance Energy Transfer (FRET) biosensor responding to the priming of LC3B by ATG4B. The biosensor was generated by flanking LC3B within a pH-resistant donor-acceptor FRET pair, Aquamarine/tdLanYFP. We here showed that the biosensor has a dual readout. First, FRET indicates the priming of LC3B by ATG4B and the resolution of the FRET image allows to characterize the spatial heterogeneity of the priming activity. Second, quantifying the number of Aquamarine-LC3B puncta determines the degree of autophagy activation. We then showed that there are small pools of unprimed LC3B upon *ATG4B* downregulation, and that the priming of the biosensor is completely abolished in *ATG4B* knockout cells. The lack of priming can be rescued with the wild-type ATG4B or with the partially active W142A mutant, but not with the catalytically dead C74S mutant. Last, we screened for commercially-available ATG4B inhibitors, and we illustrated their differential mode of action by implementing a spatially-resolved, broad-to-sensitive analysis pipeline combining FRET and the quantification of autophagic puncta. Therefore, the LC3B FRET biosensor paves the way for a highly-

31 quantitative monitoring of the ATG4B activity in living cells and in real time, with  
32 unprecedented spatiotemporal resolution.

33

34 Keywords: autophagy, LC3B, ATG4B, FRET/FLIM, biosensor

---

## 35 **Introduction**

36 Conserved in all eukaryotic cells, macroautophagy/autophagy is the lysosome-mediated degradation and  
37 recycling of the intracellular components [1]. Autophagy is triggered as a survival response in paradigms such  
38 as starvation, pathogen infection or DNA damage, and it contributes to cellular differentiation, immunity,  
39 aging and cell death [2–4]. In mammals, autophagy starts at sites of endoplasmic reticulum (ER) enriched for  
40 phosphatidylinositol 3-phosphate [PI(3)P]. On these subdomains, a double-membrane structure termed  
41 phagophore forms [5]. As the phagophore elongates into a crescent-shaped structure, it engulfs bulk or  
42 selective cargoes and then closes into a double-membrane vesicle, the autophagosome. The fusion of  
43 autophagosomes with lysosomes results in the degradation of the sequestered cargo by the lysosomal acid  
44 hydrolases.

45 A series of AuTophagy-related (ATG) proteins regulate the autophagic pathway [6]. Among them, a  
46 special attention is given to the ATG8 family, which are the key proteins found on autophagosomal  
47 membranes at all stages of the pathway. ATG8 proteins are ubiquitin-like adaptor proteins involved in  
48 autophagosome formation, biogenesis and cargo selection [7–9]. In mammals, ATG8 proteins belong to two  
49 subfamilies, the MAP1LC3/LC3 (microtubule-associated protein 1 light chain 3) and GABARAP (gamma-  
50 aminobutyric acid [GABA] type A receptor-associated protein) [10,11]. A total of seven genes - *LC3A*, *LC3B*,  
51 *LC3B2*, *LC3C*, *GABARAP*, *GABARAPL1* and *GABARAPL2* - code for the LC3 and GABARAP subfamilies  
52 in humans [10]. LC3/GABARAPs are found as inactive pro- forms upon translation, and are activated by the  
53 ATG4 family of cysteine proteases [12,13]. In humans, four members of the ATG4 family (ATG4A, B, C and  
54 D) are responsible for this activation step, which is to proteolytically cleave the C-terminus of pro-  
55 LC3/GABARAP proteins and convert them into the so-called form-I. This crucial cleavage is known as “pro-

56 LC3/GABARAP priming”, and it is essential to expose a specific glycine residue required for the lipidation  
57 of the cytosolic LC3/GABARAP-I proteins to the phosphatidylethanolamine (PE) head groups of the forming  
58 phagophores. This is achieved after a series of reactions that involves the E1-like enzyme ATG7, the E2-like  
59 enzyme ATG3 and the E3-like complex ATG12–ATG5-ATG16L1 [12,14–16]. The PE-conjugated  
60 LC3/GABARAP proteins are then called LC3/GABARAP-II, and function in membrane tethering,  
61 hemifusion, autophagosome formation and cargo recruitment [17–20]. Once the phagophore is fully closed,  
62 LC3/GABARAP-II proteins are removed from the outer surface of the phagophore membrane by ATG4s,  
63 through the hydrolysis of the link between PE and LC3/GABARAP [12]. Although the importance of this  
64 second round of cleavage activity (referred as deconjugation hereafter) by ATG4 was shown to be important  
65 for the normal progression of autophagy in yeast [21–23], recent studies in human cells suggest the existence  
66 of autophagy-independent roles for the deconjugation activity of ATG4s [24,25]. Therefore, the relevance of  
67 ATG4-mediated deconjugation for the progression and completion of autophagy in models other than yeast  
68 still requires further investigation [21–26].

69 Autophagy plays an essential role to maintain cellular homeostasis, and its dysfunction has been  
70 implicated in many pathological conditions such as neurodegenerative diseases, cancer, inflammation,  
71 muscular and hearth disorders [27]. As a consequence, therapeutic options to modulate autophagy emerged as  
72 promising strategies for the treatment of these complex pathologies [28]. In this light, targeting ATG4s to  
73 inhibit autophagy in its early stages has a significant potential to completely block autophagy [29]. However,  
74 currently available compounds targeting ATG4 activity show poor specificity and/or efficacy [30]. In addition,  
75 there is a lack of dedicated probes that can be used in living cells to monitor ATG4 activity during autophagy  
76 progression. Overall, this creates a bottleneck for the identification of ATG4 inhibitors with improved  
77 properties. For these reasons, we developed a Förster’s Resonance Energy Transfer (FRET) biosensor, named  
78 the LC3B biosensor, to simultaneously monitor: 1) the priming of LC3B by ATG4 and 2) the accumulation  
79 of LC3B on the autophagic membranes.

80 The FRET phenomenon is a non-radiative energy transfer between a donor and an acceptor pair of  
81 fluorophores. FRET can occur when the emission spectrum of the donor fluorophore partially overlaps with  
82 the excitation spectrum of the acceptor, and this only when the two fluorescent moieties are in close proximity  
83 (less than 10 nm apart) [31]. This phenomenon can be used to monitor many different cellular events including  
84 the exploration of protein-protein interactions, the changes in conformation of proteins, and the up- or  
85 downregulation of signaling pathways [32,33]. With the recent advances, FRET quantification by fluorescence  
86 lifetime imaging microscopy (FLIM) became a very useful method to study molecular activities in living cells  
87 [34].

88 In this study, we present the LC3B biosensor as a superior probe that can be used in living cells to  
89 monitor the activation – LC3B priming by ATG4 – and progression – LC3B accumulation on the autophagic  
90 membranes – of autophagy, in real time and with high spatial resolution. We show that the biosensor  
91 recapitulates the main features of the endogenous LC3B protein in terms of forming puncta-shaped structures,  
92 of ATG4B-dependent cleavage, and of its colocalization with lysosomal proteins upon autophagy induction  
93 and/or lysosomal inhibition. We also show that the biosensor can report on the changes in proLC3B priming,  
94 and this in an ATG4B-dependent manner. Using *ATG4* knockout cells, we demonstrate that the absence of  
95 ATG4B maximizes the FRET response of the biosensor as a consequence of the complete lack of proLC3B  
96 priming. We then show that proLC3B priming can be rescued with the ectopic expression of the wild-type  
97 ATG4B. Interestingly, we demonstrate that the ATG4B<sup>W142A</sup> mutant, previously shown to possess a  
98 significantly reduced catalytic activity [35], is capable of rescuing proLC3B priming similarly to the wild-  
99 type protein. By using the LC3B biosensor and performing multiple approaches to analyze FRET/FLIM, we  
100 report on the action of mechanisms of available ATG4 inhibitors. By doing so, we provide a framework of  
101 how to use the LC3B biosensor and analyze the acquired data to identify new ATG4 inhibitors with better  
102 specificity and efficacy.

## 103 **Results**

### 104 *The LC3B biosensor dynamically reports on the activation or the inhibition of the autophagy flux, and it* 105 *colocalizes with LAMP2 in an autophagy-dependent manner*

106 To monitor the priming activity of ATG4 in real time and with spatial resolution, we developed a FRET-based  
107 biosensor that can be utilized in living cells. We chose LC3B as it is a known target of the ATG4 activity that  
108 undergoes an ATG4-mediated cleavage on Gly120, and it is among the best characterized players of the  
109 autophagy pathway [36]. The biosensor was designed to flank the N- and C-termini of proLC3B with a donor-  
110 acceptor FRET pair (Fig. 1A). The FRET pair composed of Aquamarine (donor, cyan) and tdLanYFP  
111 (acceptor, yellow) was selected on the resistance of both fluorophores to acidic pH [37–39]. In the absence of  
112 ATG4 activity, the LC3B biosensor is expected to remain unprocessed in cells, allowing Aquamarine and  
113 tdLanYFP to perform FRET (Fig. 1A). If ATG4 is active, the biosensor is expected to undergo an ATG4-  
114 dependent proteolytic cleavage at its C-terminus, thereby losing the tdLanYFP moiety and the FRET effect  
115 with it. This allows to follow the initial C-terminal priming activity of ATG4 as an early, FRET-based readout.  
116 In addition, the priming of LC3B leads to its conversion into the I form, which will still be tagged by  
117 Aquamarine (Aquamarine-LC3B-I). When the resulting Aquamarine-LC3B-I protein is integrated into the PE  
118 head groups of the phagophores, the biosensor is expected to function as a canonical fluorescent probe to  
119 quantify LC3B-positive puncta structures. Therefore, our biosensor also provides a quantitative readout on  
120 the late stages of the autophagic pathway, and it can be used to estimate the number of autophagosomes in  
121 individual cells (Fig. 1A).

122 We first explored whether the LC3B biosensor is capable of localizing to autophagosomes, which  
123 normally appear as puncta-shaped structures. In U2OS cells transiently transfected to express the biosensor,  
124 Aquamarine was observed to be present both in puncta-shaped structures, which are compatible with LC3B-  
125 II, and in the cytosol, which is compatible with Aqua-LC3B-I (Fig. 1B). To confirm that the puncta-shaped  
126 structures were autophagosomes, cells were treated with autophagy inducers as Torin1 or HBSS, in the

127 presence or absence of the lysosomal inhibitor Bafilomycin A<sub>1</sub> (BafA<sub>1</sub>). Compared to control cells, a  
128 significant increase in the number of Aquamarine-positive puncta was observed in cells expressing the wild-  
129 type LC3B biosensor (WT biosensor) and treated with BafA<sub>1</sub> or Torin1 alone (Fig. 1B, C). A further increase  
130 in the number of Aquamarine-positive puncta was observed when cells were treated simultaneously with  
131 BafA<sub>1</sub> and Torin1. This indicates that the puncta-shaped structures observed under these conditions are  
132 Aquamarine-LC3B-II (Aqua-LC3B-II)-positive autophagosomes, since they respond to autophagy induction  
133 and to lysosomal inhibition alone or in combination. Conversely, autophagy induction by starvation did not  
134 cause any increase in the number of puncta-shaped structures when compared to the control (Fig. 1B, C).  
135 However, when starvation with HBSS was coupled with BafA<sub>1</sub> treatment, we observed a significant  
136 accumulation of puncta-shaped structures (Fig. 1B, C). In all conditions tested, tdLanYFP appeared to be  
137 diffused in the cytosol, thereby showing a dramatic difference compared to the distribution of Aquamarine  
138 into puncta-shaped structures. This strongly suggests that tdLanYFP is cleaved along with the C-terminal part  
139 of proLC3B, and therefore it cannot colocalize with Aquamarine on the puncta-shaped structures. To  
140 corroborate this observation, we explored the distribution of an uncleavable variant of the LC3B biosensor,  
141 which is mutated on Gly120 (hereby, G120A biosensor) and cannot be primed by ATG4 [36]. In cells  
142 expressing the G120A biosensor, both Aquamarine and tdLanYFP were exclusively diffused in the cytosol  
143 (Fig. S1), and they exhibited no puncta-shaped structures under any treatment (Fig. 1C and S1). The difference  
144 in puncta numbers between the WT and the G120A biosensors supports the notion that the WT construct is  
145 cleaved at the C-ter, and that it efficiently forms autophagosome-related puncta structures. In this light, we  
146 verified the cleavage profiles of the WT and G120A biosensors by western blotting. While the G120A  
147 biosensor had a molecular weight of ~95 kDa – corresponding to Aquamarine + proLC3B<sup>G120A</sup> + tdLanYFP  
148 –, the WT biosensor was cleaved in all conditions tested and appeared as two bands at ~45kDa and ~43kDa.  
149 These bands were compatible with the molecular weight of Aquamarine + LC3B-I at ~45 kDa, and of  
150 Aquamarine + LC3B-II at ~43 kDa (Fig. 1E). Consistent with the quantifications of puncta numbers in cells  
151 expressing the WT biosensor (Fig. 1B, C), the levels of the Aqua-LC3B-II band increased upon BafA<sub>1</sub> or

152 Torin1 treatment, but remained unaltered upon starvation with HBSS (Fig. 1E, F). A further increase in Aqua-  
153 LC3B-II abundance was observed upon the co-treatment with BafA<sub>1</sub> and Torin1 when compared to BafA<sub>1</sub> or  
154 Torin1 alone (Fig. 1E, F). Similarly, the combination of HBSS and BafA<sub>1</sub> increased the levels of Aqua-LC3B-  
155 II when compared to HBSS alone (Fig. 1E, F). These findings suggest a rather rapid degradation of Aqua-  
156 LC3B-II via lysosomal turnover in U2OS cells upon starvation with HBSS. This also suggests that the  
157 degradation of Aqua-LC3B-II can be slowed down when starvation is coupled with a late-stage lysosomal  
158 inhibitor such as BafA<sub>1</sub>. This was previously reported to occur in several other cell lines [24,40,41], and it  
159 substantiates the importance of measuring the autophagy flux in the absence or presence of lysosomal  
160 inhibitors. The differences observed in the levels of Aqua-LC3B-II were also observable at the level of the  
161 endogenous LC3B-II, confirming that the lipidation levels of the LC3B biosensor are similar to those of  
162 endogenous protein upon autophagy induction and/or lysosomal inhibition (Fig. 1E, G).

163 To provide conclusive evidence that Aqua-LC3B-II puncta structures are autophagosomes and are  
164 capable of colocalizing with lysosomes, we analyzed their colocalization with the lysosomal protein  
165 Lysosomal Associated Membrane Protein 2 (LAMP2). Compared to control cells, we found that the  
166 colocalization of Aqua-LC3B-II puncta structures with LAMP2-positive objects significantly increased when  
167 autophagy is induced with Torin1, but not with HBSS (Fig. 1B, D). As expected in cells expressing the WT  
168 biosensor, we observed that treatment with BafA<sub>1</sub> significantly reduced the colocalization of Aqua-LC3B-II  
169 puncta with LAMP2 compared to untreated, Torin1- or HBSS-treated cells. Conversely, the G120A biosensor  
170 did not colocalize with LAMP2 in any condition (Fig. 1D and S1). Overall, these results show that the WT  
171 biosensor colocalizes with LAMP2 in an autophagy-dependent manner.

172 Taken together, these results demonstrate that the LC3B biosensor is efficiently cleaved. The biosensor  
173 is capable of forming puncta structures that are consistent with the lipidated, Aqua-LC3B-II form, and they  
174 colocalize with the lysosomal protein LAMP2. The autophagy-dependent changes in the number of puncta-  
175 shaped structures or their degree of colocalization with LAMP2 indicate that the biosensor is capable of  
176 successfully reporting on autophagy induction and/or lysosomal inhibition.

## ***The LC3B biosensor responds to the changes in proLC3B priming in an ATG4B-dependent manner***

After establishing that the biosensor behaves like endogenous LC3B in cells, we sought to assess its capacity to dynamically report on LC3B processing. To this end, live cells expressing the WT or the uncleavable G120A biosensor were analyzed using FRET/FLIM. We compared the donor (Aquamarine) lifetime differences between the donor-only and the biosensor to detect FRET events, which are highlighted when the donor lifetime decreases. We then used  $\Delta$ Lifetime as a readout for FRET/FLIM analyses, which was determined by calculating the net difference between the lifetime of the donor-only construct (Aquamarine-proLC3B) and that of a biosensor (either Aquamarine-proLC3B- or proLC3B<sup>G120A</sup>-tdLanYFP). We hypothesized that a positive  $\Delta$ Lifetime would be indicative of a FRET event between Aquamarine and tdLanYFP, therefore corresponding to the presence of unprimed proLC3B.

First, we measured the FRET/FLIM readout of the WT biosensor by calculating its mean  $\Delta$ Lifetime in the total cell area. This includes the cytosol and the puncta structures, in which the precursor, primed and lipidated forms of LC3B are expected to be present. We observed that no FRET was occurring in control cells, as illustrated by a  $\Delta$ Lifetime difference close to zero (Fig. 2A, B). This indicates that the LC3B biosensor is completely primed under basal conditions, leading to the loss of the tdLanYFP moiety. Conversely, the uncleavable G120A biosensor reported a significant increase of  $\sim$ 500 psec in  $\Delta$ Lifetime compared to the WT biosensor. This led us to conclude that the FRET readout of the LC3B biosensor is directly linked to its cleavage on G120. In addition, the FRET readout is specific to the biosensor constructs, as we observed no difference in  $\Delta$ Lifetime between the WT and G120A donor-only constructs (Fig. S2A, B).

We then reasoned that the direct correlation between FRET and priming should make the LC3B biosensor responsive to the presence or absence of ATG4. To this end, we used siRNA-mediated gene silencing to downregulate the *ATG4B* isoform, as it exhibits the highest catalytic efficiency towards LC3B compared to the other members of the ATG4 family [42]. First, we verified the efficiency of the siRNA-mediated downregulation strategy by western blotting, in cells expressing the WT or the G120A biosensor (Fig. S2C, D). When comparing the mean  $\Delta$ Lifetime values, no difference was observed in cells expressing

the G120A biosensor under any condition, as expected (Fig. 2A, B). Although no difference in mean  $\Delta$ Lifetime was observable in control or *ATG4B*-depleted cells expressing the WT biosensor (Fig. 2A, B), we noticed the presence of a significant subset of pixels exhibiting high  $\Delta$ Lifetime values only in *ATG4B*-depleted cells (Fig. 2A, enlarged  $\Delta$ Lifetime image of the WT biosensor with *ATG4B* siRNA). Therefore, we hypothesized that these pixels might correspond to unprimed proLC3B. To verify our hypothesis, we ascertained that these pixels could be retrieved only upon *ATG4B* downregulation, and that they could represent unprimed pools of LC3B by showing a G120A-like FRET. To this end, we performed a pixel-by-pixel FRET/FLIM analysis to quantify the number of pixels showing  $\Delta$ Lifetime values similar or higher than the mean  $\Delta$ Lifetime of the G120A biosensor. Indeed, *ATG4B* silencing caused a significant increase in the number of pixels with high  $\Delta$ Lifetime values compared to the control condition (Fig. 2C). We then used the power of FRET microscopy to visualize these high  $\Delta$ Lifetime pixels with a line analysis. This analysis allows to observe the local variations in  $\Delta$ Lifetime occurring in the pixels crossed by a straight line.  $\Delta$ Lifetime values along the line went from zero to the levels of the G120A biosensor only in cells silenced for *ATG4B* (Fig. 2A, D). This indicates a lack of proLC3B cleavage occurring locally, and it substantiates the role of *ATG4B* in this process. We also noticed that the increase in  $\Delta$ Lifetime was localized in pixels found on or near the puncta-shaped structures (Fig. 2A). This reveals the spatial heterogeneity of the priming activity in these areas and uncovers a possible spatial regulation of proLC3B priming, which may be taking place in discrete regions in the vicinity of autophagosomes. When we performed the same analysis for donor-only constructs, we could not detect any high  $\Delta$ Lifetime pixels, ensuring that the effect that we observe with the WT biosensor upon *ATG4B* downregulation was not due to an intrinsic change in the lifetime properties of Aquamarine (Fig. S2E). To make sure that the heterogeneity of  $\Delta$ Lifetime pixels was correctly estimated in the different conditions, we analyzed the data to visualize the  $\Delta$ Lifetime distribution. We hypothesized that the presence of high  $\Delta$ Lifetime pixels with G120A biosensor-like  $\Delta$ Lifetime values should change the overall  $\Delta$ Lifetime distribution. To this end, we superimposed the histograms of the cells expressing the WT biosensor with or without *ATG4B* depletion, and we observed a shift in the histogram mode values of *ATG4B*-depleted cells towards higher

227  $\Delta$ Lifetime values (Fig. 2E). Since the mode value of a histogram corresponds to the value with the highest  
228 frequency, a positive shift in the mode indicates that the  $\Delta$ Lifetime distribution changes due to the presence  
229 of FRET events in the biosensor.

230 Considering that, in addition to its priming activity, ATG4B also acts as a deconjugating enzyme that  
231 governs the ATG8ylation levels [25,43], we checked if its depletion is causing an increase in the puncta-  
232 shaped structures. In cells expressing the WT biosensor or donor, we observed a robust increase in the number  
233 of LC3B puncta upon *ATG4B* downregulation compared to controls (Fig. 2F, S2F). This indicates that the  
234 formation of puncta-shaped structures depends on the presence of ATG4B. As expected, no puncta were  
235 observed in cells expressing the G120A biosensor or donor, regardless of the presence or absence of ATG4B  
236 (Fig. 2F, S2F). Similarly, when we analyzed protein levels by western blotting, we detected a significant  
237 increase in the lipidated levels of the biosensor (Aqua-LC3B-II) and of the endogenous LC3B-II upon *ATG4B*  
238 downregulation, compared to the controls (Fig. S2C, D).

239 Taken together, these results show that the LC3B biosensor allows to visualize changes in the ATG4B-  
240 dependent priming of proLC3B. We provide evidence that the biosensor can form LC3B puncta in an ATG4B-  
241 dependent manner, demonstrating that our probe recapitulates the key features of endogenous LC3B. Last, we  
242 demonstrate that analyzing the FRET response of the biosensor with different modalities allows to monitor  
243 the cleavage of proLC3B both at the cellular and at the subcellular level. Our findings support the pertinence  
244 of this tool to spatiotemporally characterize LC3B processing in cells.

### 246 ***The total depletion of ATG4B maximizes the FRET response of the LC3B biosensor***

247 To deepen our understanding of the mode of action of the LC3B biosensor in cells, we used *ATG4* knockout  
248 (KO) HeLa cells generated by Agrotis *et al.* using CRISPR/Cas9-mediated approaches [24]. First, we  
249 measured the FRET response of the WT or G120A biosensor expressed in control cells. Similarly to what  
250 observed in U2OS cells (Fig. 2A, B), the WT biosensor displayed a  $\Delta$ Lifetime close to zero, while the FLIM  
251 readout of the cleavage-deficient G120A biosensor showed a  $\sim$ 400 psec  $\Delta$ Lifetime (Fig. 3A, B). When looking

252 at the distribution of the two sensors, we observed that the WT biosensor was capable of forming puncta-like  
253 structures while the G120A biosensor showed a cytosolic distribution as expected (Fig. 3A). Overall, the  
254 FRET behavior and the distribution of the WT and G120A LC3B biosensors were consistent with our previous  
255 observations in U2OS cells.

256 We then sought to explore the FRET/FLIM readout of the LC3B biosensor in cells completely devoid  
257 of the ATG4 protease. We expressed the WT biosensor in *ATG4B* single knockout (SKO) HeLa cells and in  
258 comparison to control cells, the WT biosensor displayed mean  $\Delta$ Lifetime values of ~400 psec under these  
259 conditions (Fig. 3A, B). These values were nearly identical to the mean  $\Delta$ Lifetime of the G120A biosensor.  
260 Similarly to the distribution of the G120A biosensor, the WT biosensor in SKO cells did not exhibit noticeable  
261 puncta-like structures, and it remained cytosolic. Therefore, these findings support the loss of priming of the  
262 WT biosensor in an *ATG4B* SKO background. The lack of priming of the LC3B biosensor was also evident  
263 in western blotting analyses (Fig. S3). The WT biosensor expressed in control cells displayed two bands  
264 corresponding to the primed and the lipidated forms of the probe, both in the ~43-45 kDa range. In contrast,  
265 the WT biosensor expressed in *ATG4B* SKO cells exhibited a single band at ~95 kDa. This band is similar to  
266 that observed in cells expressing G120A biosensor, therefore reinforcing the conclusion that the WT biosensor  
267 remains unprimed in cells lacking the ATG4B protease. We observed that the complete knockout of *ATG4B*  
268 also abolishes the priming of endogenous LC3B, which exhibits a single band at 15 kDa compatible with  
269 unprimed proLC3B [44] (Fig. S3). These results indicate that ATG4B is indispensable for the priming and the  
270 lipidation of the LC3B biosensor.

271 We then verified whether the A and C isoforms of ATG4 family could further contribute to the priming  
272 of the LC3B biosensor. The mean  $\Delta$ Lifetime values (Fig. 3A, B) and the western blotting profiles (Fig. S3) of  
273 the WT biosensor expressed in *ATG4A/B* double knockout (DKO) or *ATG4A/B/C* triple knockout (TKO) HeLa  
274 cells [24] showed no differences compared to the *ATG4B* SKO condition. This substantiates previous *in vitro*  
275 reports showing that the catalytic activity of ATG4B is maximized towards LC3B [45]. To rule out every  
276 possibility that the A or C isoforms could still contribute to the priming of LC3B to some extent, we increased

277 the sensitivity of our analyses by performing pixel-by-pixel FRET/FLIM calculations. We quantified the  
278 number of pixels with  $\Delta$ Lifetime values similar or higher than the  $\Delta$ Lifetime of the G120A biosensor in  
279 control, *ATG4B* SKO, *ATG4A/B* DKO or *ATG4A/B/C* TKO cells. With this, we aimed to explore subtle  
280 changes possibly occurring between the KO cells that may remain undetected in mean  $\Delta$ Lifetime analyses. As  
281 expected, we observed a significant increase in the number of pixels with high  $\Delta$ Lifetime in *ATG4B* SKO cells  
282 expressing the LC3B biosensor when compared to control cells, further corroborating the results obtained with  
283 mean  $\Delta$ Lifetime analyses (Fig. 3C). However, these analyses did not highlight any significant increase in the  
284 number of pixels with high  $\Delta$ Lifetime upon further loss of *ATG4A* or *ATG4C* (Fig. 3C). Interestingly,  
285 *ATG4A/B* DKO cells showed a slight shift towards higher  $\Delta$ Lifetime values in their respective histogram mode  
286 value compared to the mode value of *ATG4B* SKO cells (Fig. 3D). However, only a negligible histogram  
287 mode value shift was observed in *ATG4A/B/C* TKO cells compared to *ATG4A/B* DKO cells. This suggests  
288 that *ATG4A* could still mildly contribute to the priming of the LC3B biosensor, although *ATG4B* is the key  
289 protease in this reaction.

290 Similarly to what observed for the endogenous LC3B protein, our results demonstrate that the priming  
291 of the LC3B biosensor is highly dependent on the presence of *ATG4B*. When *ATG4B* is absent, the LC3B  
292 biosensor displays a significant FRET response, it remains unprimed and cannot be lipidated to form puncta-  
293 like structures, overall resembling the behavior of the cleavage- and lipidation-deficient G120A biosensor.

### 295 ***The ectopic expression of active ATG4B rescues the priming deficiency of the LC3B biosensor in ATG4B-*** 296 ***deficient cells***

297 After demonstrating that the priming of the LC3B biosensor is *ATG4B*-dependent, we then asked whether its  
298 FRET response in *ATG4B*-deficient cells could be rescued by re-expressing *ATG4B*. To this end, we co-  
299 expressed the LC3B biosensor together with an empty vector or with a vector coding for WT *ATG4B*. Then,  
300 we evaluated the FRET/FLIM behavior of these conditions both in control and in *ATG4B* SKO cells.

301 Consistent with our previous findings (Fig. 3), the LC3B biosensor co-expressed with an empty vector in  
302 *ATG4B* SKO cells showed a significant increase in its mean  $\Delta$ Lifetime values compared to control cells (Fig.  
303 4A, B). Conversely, the expression of WT *ATG4B* in *ATG4B* SKO cells caused a drastic decrease in the mean  
304  $\Delta$ Lifetime values of the LC3B biosensor, which were close to zero. This suggests that the reintroduction of  
305 WT *ATG4B* is sufficient to fully rescue the cleavage of the LC3 biosensor in a SKO background. Upon the  
306 expression of exogenous *ATG4B* in control cells, we also observed that the distribution of the biosensor was  
307 cytosolic and without significant puncta-like structures (Fig. 4A). On the contrary, control cells co-expressing  
308 an empty vector were capable of forming puncta-like structures. This is in agreement with previous reports  
309 showing that the overexpression of exogenous *ATG4B* blocks the lipidation of LC3B and by doing so, it leads  
310 to the disappearance of LC3-positive puncta in cells [13,46,47].

311 Next, we assessed whether two mutant forms of *ATG4B* with different catalytic activities could rescue  
312 the priming deficiency of the LC3B biosensor in *ATG4B* SKO cells. We first explored the consequences of  
313 mutating the Cys74 residue of *ATG4B* into Ser (C74S). Cys74 belongs to a group of three aminoacids known  
314 as the “catalytic triad”, and its mutation into Ala or Ser was shown to cause a complete loss of the catalytic  
315 activity of *ATG4B* [13,35]. When *ATG4B*<sup>C74S</sup> was co-expressed with the LC3B biosensor in *ATG4B* SKO  
316 cells, we measured a mean  $\Delta$ Lifetime comparable to *ATG4B* SKO cells transfected with an empty vector (Fig.  
317 4A, B). This indicates that the catalytically-dead C74S mutant was unable to cleave and, by consequence  
318 prime, the LC3B biosensor. We then tested a second mutant form of *ATG4B* where Trp142 was mutated into  
319 Ala (W142A). Trp142 is one of the residues surrounding the catalytic triad, and its mutation into Ala was  
320 reported to significantly reduce the catalytic activity of *ATG4B in vitro* [35]. Surprisingly, we observed that  
321 *ATG4B*<sup>W142A</sup> behaved similarly to WT *ATG4B* when expressed in SKO cells, and it resulted in a complete  
322 cleavage of the LC3B biosensor in FRET/FLIM analyses (Fig. 4A, B). This supports the superior catalytic  
323 efficiency of *ATG4B* to prime proLC3B in living cells, even in conditions where its catalytic activity is  
324 severely compromised by the W142A mutation. To verify that these changes in mean  $\Delta$ Lifetime were specific  
325 to the LC3B biosensor, we analyzed the mean  $\Delta$ Lifetime profiles of control or *ATG4B* SKO cells expressing

326 the donor-only Aquamarine-LC3B construct together with WT, C74S or W142A ATG4B (Fig. S4A). As  
327 expected, we did not observe any difference among all the conditions tested, further confirming that the mean  
328  $\Delta$ Lifetime FRET/FLIM readout is specific towards the ATG4B-mediated cleavage of the LC3B biosensor.

329 We then wanted to verify if our approach based on mean  $\Delta$ Lifetime was sensitive enough to conclude  
330 on the capacity of the W142A mutant to fully prime LC3B. Therefore, we further evaluated the readout of the  
331 LC3B biosensor by performing pixel-by-pixel FRET/FLIM calculations, which we previously showed to be  
332 more sensitive than mean  $\Delta$ Lifetime analysis (Fig. 2). As expected, we observed a significant increase in the  
333 number of pixels with high  $\Delta$ Lifetime – indicating no LC3B priming – in *ATG4B* SKO cells co-expressing an  
334 empty vector or *ATG4B*<sup>C74S</sup> compared to control cells (Fig. 4C). Similarly to mean  $\Delta$ Lifetime analyses (Fig.  
335 4B), expressing WT *ATG4B* or *ATG4B*<sup>W142A</sup> in *ATG4B* SKO cells revealed an absence of pixels with high  
336  $\Delta$ Lifetime values, suggesting a complete rescue of the priming activity of the LC3B biosensor with both  
337 constructs (Fig. 4C). Accordingly, the histogram analyses of the distribution of FRET pixels in all conditions  
338 showed almost identical mode values in *ATG4B* SKO cells co-expressing WT or *ATG4B*<sup>W142A</sup>, with their  
339 respective mode values centered around zero (Fig. 4D). On the contrary, the mode values of *ATG4B* SKO  
340 cells expressing an empty vector or *ATG4B*<sup>C74S</sup> were drastically shifted towards 400 psec, which is again  
341 indicative of significant FRET (Fig. 4D). As expected, the analysis of the high  $\Delta$ Lifetime pixels in control or  
342 SKO cells expressing the donor-only Aquamarine-LC3B and each of the *ATG4B* constructs did not reveal  
343 any difference (Fig. S4B). Again, this substantiates the specificity of our different FRET/FLIM readouts for  
344 the LC3B biosensor only. In addition to this, the WT biosensor expressed in control cells with each of the  
345 *ATG4B* constructs exhibit similar histogram mode values (Fig. S4C). Nevertheless, we observed the presence  
346 of a shoulder corresponding to  $\Delta$ Lifetime values of ~200-300 psec in control cells co-expressing the WT  
347 biosensor with *ATG4B*<sup>C74S</sup> (Fig. S4C), which could reflect the previously reported dominant negative effects  
348 of *ATG4B*<sup>C74S</sup> on the soluble forms of LC3B [46].

349 Altogether, our results demonstrate that the proLC3B priming deficiency observed in *ATG4B* SKO  
350 cells can be fully restored when co-expressing the WT or W142A forms of *ATG4B*, but not with the

351 catalytically-dead C74S. Although ATG4B<sup>W142A</sup> was shown to display a reduced catalytic activity *in vitro*  
352 [35], we demonstrate that this mutant is able to prime proLC3B in living cells similar to WT ATG4B. These  
353 data were obtained with three independent methods to calculate the FRET behavior of the LC3B biosensor,  
354 and they provide novel insights on the superior capacity of ATG4B to prime LC3B *in cellulo* even in  
355 conditions where its catalytic activity is compromised. Importantly, they also support the notion that the  
356 catalytic activity of ATG4B needs to be completely eliminated to abolish LC3B priming.

### 357 358 ***The LC3B biosensor reveals the mode of action of ATG4 inhibitors in cells***

359 Given that the biosensor reports on the priming of LC3B by ATG4B, we sought to investigate whether it is  
360 also capable to respond to pharmacological compounds that inhibit the ATG4B-LC3B axis. We first explored  
361 the effect of MG132, a peptide aldehyde that inhibits both the proteasome and cysteine proteases [48,49].  
362 Considering that ATG4B is a cysteine protease [14,35], we reasoned that MG132 might be able to block its  
363 catalytic activity towards LC3B. Therefore, we treated HeLa cells expressing the WT or G120A biosensor  
364 with DMSO or MG132, and calculated their mean  $\Delta$ Lifetime (Fig. S5A, B). FLIM analyses revealed a  
365 significant increase in the mean  $\Delta$ Lifetime values of the WT biosensor in the presence of MG132. We reasoned  
366 that MG132 could promote FRET within the biosensor either by inhibiting the priming activity of ATG4B, or  
367 by inhibiting LC3B degradation by the proteasome. To distinguish between these two possibilities, we relied  
368 on the subcellular distribution of the biosensor. In this light, the biosensor should be retrieved in the cytosol  
369 in case MG132 had mainly an ATG4B-specific inhibition on proLC3B priming. Alternatively, it should rather  
370 be found in puncta-like structures if this drug acted as a proteasome inhibitor. We observed a significant  
371 increase in the number of Aqua-LC3B-II puncta-like structures in cells expressing the WT biosensor and  
372 treated with MG132, when compared to DMSO-treated cells (Fig. S5B). Therefore, this localization of the  
373 sensor in puncta-like structures suggests that MG132 is more efficient as a proteasome inhibitor, rather than a  
374 specific ATG4B inhibitor. Although the number of pixels with high  $\Delta$ Lifetime values did not significantly  
375 increase upon MG132 treatment (Fig. S5B), the histogram analysis of MG132-treated cells expressing the WT

376 biosensor revealed a mode value change when compared to DMSO-treated cells and to cells expressing the  
377 G120A biosensor (Fig. S5C). Overall, this indicates that FRET events are quantitatively modest in the  
378 presence of MG132, suggesting that MG132 preferentially acts as a proteasomal inhibitor rather than an  
379 ATG4B-specific inhibitor. Although FRET events were limited under these conditions, we sought to explore  
380 their spatial localization. Line analyses performed in cells expressing the WT biosensor and treated with  
381 MG132 revealed that the  $\Delta$ Lifetime variations of the biosensor were of  $\sim$ 200 psec in the cytosol, and reaching  
382  $\Delta$ Lifetime values of the G120A biosensor ( $\sim$ 400 psec) on or near the LC3B puncta (Fig. S5B, D). In contrast,  
383 no fluctuations were observed in the cytosol or near puncta in control cells. These two FRET values observed  
384 after treating cells with MG132 could be recapitulative of the dual action of this compound: a modest ATG4B  
385 inhibitor keeping the biosensor in the cytosol, and a more potent proteasomal inhibitor on LC3B-positive  
386 puncta. Of note, since Aqua-LC3B can efficiently localize on puncta-like structures (Fig. S5B) which display  
387 high FRET (Fig. S5B, D), our data raise the possibility that MG132 does not alter the cleavage of tdLanYFP  
388 from the biosensor. It is possible that the inhibition of proteasomal activity impairs the degradation of the  
389 FRET acceptor, thereby allowing for non-specific FRET events. Therefore, these results underline the  
390 importance of performing spatially-resolved, pixel-by-pixel FRET calculations to understand where and to  
391 what extent the biosensor is active. They also highlight the poor efficacy of MG132 as an ATG4B-specific  
392 inhibitor.

393         Afterwards, we explored the readout of the LC3B biosensor on commercially-available inhibitors with  
394 better specificity than MG132 towards ATG4. Tioconazole, LV-320, FMK-9a, NSC 185058 (NSC) and *Z-L*-  
395 Phe chloromethyl ketone (ZPCK) were evaluated in their capacity to inhibit the priming and/or deconjugation  
396 activities of ATG4B [50–55]. These inhibitors have either been synthesized or identified in screening studies,  
397 and they were previously shown to inhibit ATG4B and/or other ATG4 isoforms. They were also reported to  
398 have a significant therapeutic potential in chemotherapy-resistant cancer subtypes with elevated levels of  
399 autophagy [29,30].

400 We first measured the mean  $\Delta$ Lifetime values in HeLa cells expressing the WT or the G120A  
401 biosensor, and treated or not with each of the five inhibitors. Based on our previous findings in *ATG4* KO  
402 cells, we expected to observe a maximized FRET response when cells are treated with the inhibitors, along  
403 with the cytosolic distribution of the WT biosensor. Within our selected set of inhibitors, two of them – NSC  
404 and ZPCK – were found to significantly increase mean  $\Delta$ Lifetime values compared to controls (Fig. 5A vs.  
405 5E, F). On the contrary, Tioconazole, LV-320 and FMK-9a did not alter the mean  $\Delta$ Lifetime values of the  
406 biosensor (Fig. 5A-D). However, the mean  $\Delta$ Lifetime values of cells treated with NSC or ZPCK remained  
407 lower than those of cells expressing the G120A biosensor. This suggests that the inhibitory effect of these  
408 drugs towards ATG4B remains partial. We then asked whether the main function of NSC and ZPCK is to  
409 inhibit the ATG4B-dependent deconjugation of LC3B or its priming. We observed a significant increase in  
410 the number of Aqua-LC3B-II puncta structures upon treatment with NSC or ZPCK, further supporting the  
411 idea that autophagy can still be triggered in the presence of these compounds and that the inhibition of ATG4B  
412 priming activity is not complete (Fig. 5E, F). However, increased levels of Aqua-LC3B-II puncta structures  
413 were observed in cells treated with Tioconazole, LV-320 or FMK-9a as well (Fig. 5B-D), and we found no  
414 correlation between puncta numbers and mean  $\Delta$ Lifetime values with any of the inhibitors (Fig. S6). These  
415 findings suggest that all the tested compounds preferentially hinder the deconjugation activity of ATG4B  
416 towards LC3B, which was described to be more sensitive to ATG4B inhibition than the priming activity [56].  
417 In addition to deconjugation, mean  $\Delta$ Lifetime differences provide the first evidence that NSC and ZPCK also  
418 inhibit the priming activity of ATG4B.

419 To dissect the efficacy of the five ATG4B inhibitors with methods allowing for greater sensitivity than  
420 mean  $\Delta$ Lifetime, we then performed high  $\Delta$ Lifetime-pixel counting and histogram analyses. The high  
421  $\Delta$ Lifetime-pixel counting analyses revealed that not only NSC and ZPCK, but also FMK-9a exhibited a  
422 significantly increased number of pixels with high  $\Delta$ Lifetime compared to control cells (Fig. 6A-D). When  
423 we analyzed the distribution of  $\Delta$ Lifetime pixels on histogram analyses, we observed that approximately 10-  
424 20% of pixels in cells treated with NSC or ZPCK were exhibiting G120A biosensor-like  $\Delta$ Lifetime values.

425 These values were lowered in the presence of Tioconazole, LV-320 and FMK-9a, further corroborating the  
426 superiority of NSC and ZPCK in inhibiting ATG4B (Fig. S7). In line with these findings, histogram analyses  
427 revealed that NSC (113 psec) and ZPCK (150 psec) have the largest histogram mode value shift from that of  
428 control cells (Fig. 6C, D). Interestingly, these analyses showed that FMK-9a, Tioconazole and LV-320 also  
429 display a mode value shift from that of control cells, respectively of 74, 65 and 47 psec (Fig. 6B, S7B-C).  
430 Therefore, this sensitive analysis method indicates a mild inhibition of the priming activity of ATG4B by  
431 FMK-9a, Tioconazole and LV-320 as well, which was undetectable with the other analysis methods.  
432 Furthermore, this approach substantiates the superior capacity of NSC and ZPCK in inhibiting ATG4B.

433 Since we observed the presence of high  $\Delta$ Lifetime pixels with all the inhibitors, we then sought to  
434 investigate the subcellular location of these pixels using line analysis. Similarly to what observed on cells  
435 silenced for *ATG4B* (Fig. 2) or treated with MG132 (Fig. S5), we noticed that high  $\Delta$ Lifetime pixels were  
436 located either on the puncta-shaped structures, or in the surrounding area (Fig. 6 and S7). Line analyses also  
437 revealed that these pixels had  $\Delta$ Lifetime values comparable to those of the G120A biosensor, regardless of  
438 the compound used. Taken together, these findings show that ATG4B inhibition using commercially-available  
439 drugs reduces the priming rates of proLC3B at discrete sites, where unprimed LC3B reservoirs can be found  
440 within or in the proximity of puncta-shaped structures.

441 Overall, our data demonstrate that the LC3B FRET biosensor is a powerful tool to evaluate the mode  
442 of inhibition of ATG4B-specific compounds. We also provide an innovative methodology where individual  
443 sets of microscopy data can be analyzed using three independent approaches. Cumulating the information  
444 obtained by the three approaches allows to spatially localize and quantify the ATG4B-dependent priming and  
445 deconjugation of LC3B with unprecedented precision, and it is mandatory to characterize the mode of action  
446 of present and future ATG4B-specific inhibitors.

447

## 448 **Discussion**

449 In this study, we demonstrated that the LC3B biosensor is a robust tool to monitor autophagy, as it responds  
450 to the priming and deconjugation activities of ATG4B on LC3B. We showed that these functions of ATG4B  
451 can be followed by using one single probe with a dual readout based on FRET, and on the accumulation of  
452 the probe on autophagosomes.

453 Among the several approaches available to monitor autophagy, the most widely used assays rely on  
454 the use of single fluorescent protein (FP)-tagged LC3B probes to quantify the number of autophagosomes  
455 [57]. The LC3B biosensor retains this property, since it functions as a standard single FP-tagged probe after  
456 LC3B is primed. We also show that the biosensor reports on autophagy induction and/or inhibition while  
457 colocalizing with the lysosomal marker protein LAMP2 in an autophagy-dependent manner, similarly to other  
458 LC3B-based fluorescent constructs. Since the LC3B biosensor is constituted of a pair of FPs resistant to acidic  
459 pH, its readout can be followed throughout the entire autophagy pathway. Importantly, the LC3B biosensor  
460 has the capacity to respond to proLC3B priming in living cells, thanks to these FPs behaving as a donor-  
461 acceptor FRET pair. The proLC3B priming by ATG4s is among the earliest events occurring when autophagy  
462 is triggered [13,36]. A FRET-based strategy relying on a CFP/YFP donor-acceptor pair has already been used  
463 to measure the enzymatic activity of ATG4A and ATG4B towards the ATG8 family in a purely *in vitro* system  
464 [58]. However, this strategy has never been implemented in living cells, most likely due to the lack of yellow  
465 FPs retaining their acceptor properties in conditions of acidic pH. The recent development of tdLanYFP [39]  
466 allowed us to create an LC3B biosensor suitable for living cells. By following the FRET behavior of the  
467 biosensor, we showed that the probe responds to the ATG4B-dependent changes in proLC3B priming. It was  
468 previously reported that proLC3B is primed nearly instantaneously after translation, due to the constitutive  
469 proteolytic activity of ATG4B [36,59]. In line with this, we found that the LC3B biosensor was almost  
470 completely primed under basal conditions, without any detectable accumulation of proLC3B in cells. In  
471 contrast, we showed that the proLC3B priming activity is altered in cells silenced for *ATG4B*, and that the

472 unprimed biosensor is located on or in close vicinity of puncta-shaped structures. Since the priming activity  
473 of ATG4B is more efficient than its deconjugation activity, alterations in ATG4B levels were shown to mostly  
474 affect deconjugation rather than priming [56]. Our findings using the LC3B biosensor were complementary  
475 to this notion, as we were able to observe a stark increase in the number of Aqua-LC3B-II puncta structures  
476 when *ATG4B* was silenced. By using a combination of broad and sensitive approaches to quantify FRET, we  
477 provided the first proof of concept that proLC3B priming events occur at discrete sites in cells. It is likely that  
478 these sites are already present to a lower extent under basal conditions, and they are highlighted only when  
479 ATG4B priming activity is altered. With microscopy approaches with higher resolution, it might be possible  
480 to reveal the existence of these reservoirs under basal conditions as well. In this light, the LC3B FRET  
481 biosensor has the unique capacity to identify these priming reservoirs in living cells and with subcellular  
482 resolution, underlining the superior sensitivity of the LC3B biosensor to explore the functional relevance of  
483 these structures and the proteins regulating their formation.

484 Furthermore, we confirmed that the isoform ATG4B is the major cysteine protease priming the LC3B  
485 biosensor, and that its knockout results in a complete lack of priming. Additionally, we provided evidence that  
486 ATG4A could mildly contribute to the priming of the LC3B biosensor in the absence of ATG4B, corroborating  
487 previous findings concerning a functional redundancy among these isoforms [24,60]. Interestingly, our  
488 biosensor provided novel information on the relevance of specific ATG4B residues for its priming activity. In  
489 this light, we observed an unexpected ability of mutant ATG4B<sup>W142A</sup> to fully prime proLC3B. Trp142 localizes  
490 near the catalytic Cys74 residue, and it was suggested to be responsible for LC3 tail recognition [35]. In *in*  
491 *vitro* cleavage assays, ATG4B with mutated Trp142 displayed a significantly reduced ability to cleave C-  
492 terminally tagged LC3 [35]. Based on these findings, we were expecting to observe a reduced LC3B priming  
493 with ATG4B<sup>W142A</sup>, and no priming was expected with the catalytically-dead mutant ATG4B<sup>C74S</sup>. While  
494 ATG4B<sup>C74S</sup> was incapable of priming proLC3B, we observed a full priming of the LC3B biosensor in the  
495 presence of the ATG4B<sup>W142A</sup> construct. Not only these results corroborate the high efficiency of ATG4B to

496 cleave proLC3B even in conditions where its catalytic activity is severely reduced, but they also highlight a  
497 drastic difference between *in vitro* findings and data obtained in more complex paradigms.

498         Given the rising interest in developing inhibitors that block the early stages of autophagy by targeting  
499 ATG4B, we challenged the LC3B biosensor with a selection of available inhibitors. Again, our biosensor  
500 demonstrated to be a useful tool to investigate the mode of action and the efficacy of these compounds at the  
501 concentrations and timepoints chosen for the analyses. First, we observed increased amounts of Aqua-LC3B-  
502 II puncta after the incubation with all the inhibitors, indicating a reduction in the deconjugation activity of  
503 ATG4B. These results were not surprising, as the deconjugation activity of ATG4B was reported to be less  
504 efficient than the priming, and therefore more prone to get affected upon inhibition [56]. Furthermore, our  
505 data also show that none of the inhibitors was able to completely abolish the priming activity of ATG4B  
506 towards LC3B. Indeed, we did not observe a cytosolic distribution of the LC3B biosensor, nor  $\Delta$ Lifetime  
507 values similar to those measured with the priming-defective G120A biosensor. Despite an incomplete  
508 inhibition on priming, we found that the cells treated with NSC or ZPCK exhibited a significant reduction in  
509 LC3B priming compared to control cells. Cells treated with MG132 – a proteasome inhibitor with a capacity  
510 to inhibit cysteine proteases [48,49] – exhibited a significant increase in the mean  $\Delta$ Lifetime values, along  
511 with a positive shift in the histogram mode value. In contrast, they did not display significant amounts of  
512 pixels with high  $\Delta$ Lifetime. It is possible that the incubation with MG132 does not prevent the complete  
513 degradation of tdLanYFP once this moiety has been cleaved from the biosensor. In this case, the presence of  
514 tdLanYFP in the close vicinity of Aqua-LC3B-II puncta would lead to unspecific FRET events, potentially  
515 unrelated to the proLC3B priming readout of the biosensor. This is the reason why a multi-parameter FRET  
516 quantification – mean  $\Delta$ Lifetime, number of pixels with high  $\Delta$ Lifetime, histogram distribution of the  
517  $\Delta$ Lifetime values – is mandatory to characterize the specificity of ATG4B inhibitors. In this light, we propose  
518 that an efficient ATG4B inhibitor should display a significant difference from controls in the three methods  
519 of analysis. A compound that did not meet all the criteria but still displayed a significant increase in the number  
520 of high- $\Delta$ Lifetime pixels with a positive histogram mode value shift was FMK-9a. Although FMK-based

521 compounds were shown to be very potent ATG4B inhibitors [30,52,61], a recent study showed that FMK-9a  
522 induces autophagy independently of its inhibition on ATG4B activity [53]. Therefore, our findings support  
523 these results since FMK-9a did not meet all the criteria to be considered as an efficient ATG4B inhibitor.  
524 Finally, our results on Tioconazole and LV-320 indicate that these two compounds inhibit the priming of  
525 proLC3B to a lesser extent than the other compounds. Since they only displayed a positive shift in the  
526 histogram mode values and did not meet any other criteria, we propose that they should be considered as mild  
527 ATG4B inhibitors. Overall, our results underline the lack of inhibitors that can fully inhibit the priming activity  
528 of ATG4B. Future screenings using the LC3B biosensor will be useful to identify new inhibitory compounds,  
529 as one would expect to observe a FRET behavior similar to that of the G120A biosensor or *ATG4* KO cells in  
530 case of a full inhibition of proLC3B priming.

531 Since it is possible to calculate the number of pixels with high  $\Delta$ Lifetime, additional information can  
532 be provided by localizing these pixels at the subcellular level. We observed a consistent presence of pixels  
533 with high  $\Delta$ Lifetime around or on puncta-shaped structures, either upon ATG4B inhibition or *ATG4B*  
534 silencing. In this light, we suggest that the local scarcity or the inhibition of ATG4B may cause alterations in  
535 the proLC3B priming rates in discrete areas of the autophagosomes, which could be considered as priming  
536 “hotspots”. As previously mentioned, these reservoirs or “hotspots” with reduced proLC3B priming rates may  
537 be sites where proLC3B is temporarily stored while trying to re-establish the full priming capacity of ATG4B.

538 Overall, we present the LC3B biosensor as a second-generation FRET biosensor that can report on the  
539 regulation of the soluble and the lipidated forms of LC3B by ATG4B. First, this tool can be used to infer on  
540 the structural properties of ATG4B and on its enzymatic activity. Thanks to its dual FRET/localization  
541 readout, it can also be used to follow LC3B priming and turnover with superior spatiotemporal resolution.  
542 Finally, the LC3B biosensor has the potential to be used in high-content screenings to identify more potent  
543 ATG4B inhibitors and reveal their mode of action in living cells, which is a unique feature of the biosensor  
544 compared to *in vitro* screening methodologies. Thus, the LC3B biosensor paves the way to ATG4B-targeted  
545 therapies in complex diseases.

## 546 **Materials and Methods**

### 547 *Expression vectors and molecular cloning*

548 All the plasmids used in this study are listed in Supplementary Table 1. The cloning reactions were performed  
549 using the Gibson Assembly Master Mix (New England Biolabs). Site-directed mutagenesis was performed  
550 with the Quik-Change kit (Agilent). All the constructs from cloning and mutagenesis reactions were verified  
551 using a 3130 XL sequencer (Applied Biosystems) and a BigDye Terminator V3.1 sequencing kit (Applied  
552 Biosystems).

### 554 *Cell culture and transfections*

555 U2OS cells (HTB-96) were purchased from American Type Culture Collection. Control and *ATG4* KO HeLa  
556 cells were kind gifts of Dr. Robin Ketteler (UCL, LMCB, United Kingdom). Cells were cultured in DMEM  
557 (Thermo Fisher Scientific) supplemented with 10% FBS (Eurobio Scientific) and penicillin-streptomycin (100  
558 U/mL, Thermo Fisher Scientific) and maintained at 37°C with 5% CO<sub>2</sub>. All cell lines were routinely checked  
559 for the absence of mycoplasma. Before imaging, normal growth media was replaced with phenol red-free  
560 Leibovitz's L-15 medium (Thermo Fisher Scientific) supplemented with 20% FBS and penicillin-  
561 streptomycin (100 U/mL). Cells were seeded at 70% confluence in Nunc Lab-Tek II Chamber slides (Thermo  
562 Fisher Scientific) or Cellview cell culture slides (Greiner bio-one, 543979) for live cell imaging, 24-well plates  
563 for immunocytochemistry, or 6-well plates for total cell lysates. Plasmid DNA transfection, or plasmid DNA  
564 and siRNA co-transfection experiments were performed using Lipofectamine 2000 (Invitrogen) according to  
565 the manufacturer's instructions. Cells were analyzed 48h after transfection. AllStars negative control siRNA  
566 (SI03650318) and the *ATG4B*-specific siRNA (SI03156314) were purchased from QIAGEN.

### 568 *Chemical compounds*

569 The chemical compounds used in this study were as follows: Bafilomycin A1 (Sigma-Aldrich, B1793), FMK  
570 9a (MedChemExpress, HY-100522), LV-320 (MedChemExpress, HY-112711), MG-132 (Selleckchem,  
571 S2619), NSC 185058 (Selleckchem, S6716), Tioconazole (Sigma-Aldrich, 03907), Torin1 (Sigma-Aldrich,  
572 475991), *Z-L-Phe* chloromethyl ketone (Sigma-Aldrich, 860794). All chemical compounds were dissolved in  
573 dimethyl sulfoxide (Sigma-Aldrich, D2438) and stored at -80°C. For starvation assay, a home-made Hank's  
574 Balanced Salt Solution (HBSS) containing 8 mg/ml NaCl, 0.4 mg/ml KCl, 0.06 mg/ml KH<sub>2</sub>PO<sub>4</sub>, 0.048 mg/ml  
575 Na<sub>2</sub>HPO<sub>4</sub> anhydrous, 1 mg/ml glucose, 0.348 mg/ml NaHCO<sub>3</sub> and penicillin-streptomycin (100 U/mL) was  
576 used. Concentrations and durations of each treatment are indicated in the figure legends.

577

### 578 ***Western blotting***

579 To collect total cell lysates, cells were rinsed with ice-cold Phosphate Buffer Saline (PBS) (Euromedex,  
580 ET330-A) and lysed on ice in a buffer containing 50 mM Tris-HCL (pH 7.4), 150 mM NaCl, 1% Triton X-  
581 100 (Euromedex, 2000-A), 1.5 mM MgCl<sub>2</sub>, supplemented with 0.2 mM Na<sub>3</sub>VO<sub>4</sub>, 0.5 mM DTT (Thermo  
582 Fisher Scientific, R0861), 4 mg/ml NaF, 5.4 mg/ml β-glycerolphosphate and a protease inhibitor cocktail  
583 (Roche, 11873580001) immediately prior to lysis. Lysates were centrifuged at 13000 g for 20 minutes at 4°C.  
584 Protein levels were quantified by using the Bradford protein assay dye reagent (BioRad, 5000006). Lysates  
585 were then heated in Laemmli sample buffer at 95°C for 5 minutes, resolved in home-made Acrylamide/Bis  
586 37.5:1 SDS-PAGE mini gels and transferred onto nitrocellulose membrane (Amersham™ Protran®,  
587 10600004). Membranes were blocked in a solution containing 5% skimmed milk in TBS-T (TBS [Euromedex,  
588 ET220] containing 0.1% Tween [Euromedex, 2001-B]) and incubated overnight at 4°C with primary  
589 antibodies diluted in the blocking solution. The next day, membrane was washed in TBS-T, incubated with  
590 the secondary antibody diluted in the blocking solution for 1h at room temperature, and washed again in TBS-  
591 T prior to detection. The primary antibodies and dilutions were as follows: rabbit anti-Actin (Sigma-Aldrich,  
592 A5060; 1:1000), ATG4B (Cell Signaling, 5299; 1:1000), LC3B (Cell Signaling, 3868; 1:1000). The secondary  
593 antibody used was a horseradish-peroxidase-conjugated goat anti-rabbit antibody (Jackson ImmunoResearch;

594 1:6000-1:10000). After incubating the membrane in an ECL western blotting substrate (Thermo Fisher  
595 Scientific, 32209), chemiluminescence signals were captured on a film (Thermo Fisher Scientific, 34091) and  
596 developed with a CURIX 60 developer (Agfa Healthcare). The density of the bands was quantified by using  
597 the *Gel Analyzer* function in Fiji (NIH) software. The relative abundance of each band was calculated by  
598 normalizing the density of the band to that of the respective loading control.

### 600 ***Immunocytochemistry, confocal and FLIM microscopy***

601 For immunocytochemistry, cells were seeded on 15 mm round coverslips placed onto 24-well plates. Cells  
602 were washed with 1X PBS and fixed in 1X PBS containing a mixture of 4% paraformaldehyde (Electron  
603 Microscopy Sciences, 15710) and 0.2% Glutaraldehyde (Euromedex, EM-16221) at room temperature for 20  
604 minutes. After washing in 1X PBS, cells were permeabilized with 0.2% Triton in PBS for 10 minutes, washed  
605 again in 1X PBS and blocked for 1h in 5% BSA (Euromedex, 04-100-812-C) in 1X PBS at room temperature.  
606 Cells were incubated overnight at 4°C with primary antibodies diluted in the blocking buffer, and then washed  
607 with 1X PBS. Cells were then incubated with the secondary antibody diluted in the blocking buffer for 45  
608 minutes at room temperature. Primary monoclonal anti-LAMP2 (Abcam, ab25631; 1:200) was used as a  
609 primary antibody and a goat anti-mouse IgG (H+L) cross-adsorbed antibody Alexa Fluor™ 647 (Thermo  
610 Fisher Scientific, A-21235; 1:500) was used as a secondary antibody. After washing in 1X PBS, coverslips  
611 were mounted in ProLong Gold Antifade reagent (Invitrogen, P36930). Cells were imaged with a Leica SP8  
612 inverted confocal microscope equipped with a 63x oil immersion objective (NA 1.4). Aquamarine  
613 fluorescence was acquired with a 440 nm excitation laser, and an emission wavelength of 467-499 nm. The  
614 fluorescence of tdLanYFP and of LAMP2/Alexa 647 were captured by using a 514 nm and a 633 nm argon  
615 laser, respectively. The emission wavelengths were 525-565 nm for tdLanYFP, and 650-720 nm for  
616 LAMP2/Alexa 647. For FLIM analyses, images were acquired with a time-gated custom-made setup based  
617 on a spinning disk microscope as described in [62]. Aquamarine was used as a FRET donor in all experiments,  
618 and excited at  $440 \pm 10$  nm with a supercontinuum picosecond pulsed laser source. Emission was selected

619 using a band pass filter of 483/35 nm. The FLIM setup was controlled by the Inscoper Suite solution (Inscoper,  
620 France), and Aquamarine lifetime was measured in real-time during acquisition with the Inscoper software.

## 622 ***Image analysis***

623 All the image analysis were performed in Fiji software. 3D puncta counting and fluorescence colocalization  
624 analyses illustrated in Fig. 1B-D and Fig. S1 were performed by using the macro developed by Cordelières  
625 and Zhang [63] in batch processing mode, and available in a GitHub repository at  
626 <https://github.com/NEUBIAS/neubias-springer-book-2020>. The minimum size of the objects for Aquamarine-  
627 LC3B and LAMP2/Alexa 647 was set to 10 voxels. The threshold to separate the objects from the background  
628 was set manually for both channels. The total number of objects in Aquamarine-LC3B channel was used to  
629 determine the number of Aqua-LC3B-II puncta-shaped structures. The objects in the Aquamarine-LC3B  
630 channel superposing with the LAMP2/Alexa 647 objects were used for colocalization analyses, and only the  
631 Aquamarine-LC3B objects superposing with the LAMP2/Alexa 647 objects with a ratio of 0.5 or more were  
632 quantified for analyses. The colocalizing objects were then normalized to the total number of Aquamarine-  
633 LC3B objects. For FLIM analysis, mean  $\Delta$ Lifetime values were calculated as previously described [38]. In all  
634 experiments, Aquamarine lifetime was calculated by the Inscoper software only when the pixel-by-pixel  
635 fluorescence intensity in the first gate was above 1000 grey levels. The number of Aqua-LC3B-II puncta  
636 structures in the accompanying fluorescence images (Fig. 2A, S2A, 5A-F, S5A-B) were quantified using the  
637 *Find Maxima* function in the Fiji imaging software, and by setting the prominence value as 1500. To analyze  
638 the high- $\Delta$ Lifetime pixels, the *Histogram* tool in Fiji was used to measure the number of pixels with a lifetime  
639 between 2000 and 4000 psec. Each histogram was then converted to a  $\Delta$ Lifetime format by using the mean  
640 lifetime value of the donor-only construct as a normalizer. To determine the number of pixels with high  
641  $\Delta$ Lifetime, the mean  $\Delta$ Lifetime value of the G120A biosensor or the mean  $\Delta$ Lifetime value of the WT  
642 biosensor expressed in *ATG4B* SKO cells were used as a threshold. The number of pixels showing G120A  
643 biosensor-like  $\Delta$ Lifetime or higher were then quantified and normalized to the total number of pixels, and this

644 to determine the high- $\Delta$ Lifetime pixel ratio per cell. For line analysis, a 17.8  $\mu\text{m}$  linear region of interest (ROI)  
645 that contains both the high- and low- $\Delta$ Lifetime pixels was manually drawn near or on the puncta-like  
646 structures. The *Plot profile* function in Fiji was then used to obtain  $\Delta$ Lifetime values on the drawn line, which  
647 were then plotted. For histogram analyses, the average number of pixels per  $\Delta$ Lifetime was quantified for each  
648 condition.

### 650 *Statistical analysis*

651 All statistical tests were performed by using GraphPad Prism 9. Two-way ANOVA with Tukey method was  
652 applied to make multiple comparisons in the following figures: 1C-D; 2B-C, F; 3B-C; 4B-C; 5B-F; 6B-D;  
653 S2B, F; S4A-B; S5B; S7B-C. Two-way ANOVA with two-stage step-up method of Benjamini, Krieger and  
654 Yekutieli was applied to make multiple comparisons in the following figures: 1F-G and S2D. Correlation  
655 analysis between the  $\Delta$ Lifetime values and the puncta numbers were performed to compute  $R^2$  and P values  
656 in Fig. S6.

### 658 *Figure preparation*

659 The cartoon in Figure 1A was prepared by using the illustrations available at <https://smart.servier.com/> [64].  
660 Graphs and figures were assembled in GraphPad Prism 9 and Inkscape, respectively.

### 662 *Data and material availability*

663 Plasmids and macro used in this study and the source data that support the findings are available from the  
664 corresponding authors (G.B. [[giulia.bertolin@univ-rennes1.fr](mailto:giulia.bertolin@univ-rennes1.fr)] and M.T. [[marc.tramier@univ-rennes1.fr](mailto:marc.tramier@univ-rennes1.fr)]) on  
665 request.

## 667 **Acknowledgments**

668 We thank P. Govindin (MetaGenoPolis, INRAe, Jouy-en-Josas, France) for preliminary experiments with the  
669 LC3B biosensor, S. Dutertre and X. Pinson at the Microscopy Rennes Imaging Center (MRic, *Biologie, Santé,*  
670 *Innovation Technologique* - BIOSIT, Rennes, France) and G. Le Marchand (IGDR, Rennes, France) for help  
671 and assistance. MRic is member of the national infrastructure France-BioImaging supported by the French  
672 National Research Agency (ANR-10-INBS-04). We also thank R. Ketteler (UCL, LMCB, United Kingdom)  
673 for sharing pGEX GST-ATG4B plasmid and *ATG4* KO HeLa cells. We are grateful to S. Ley-Ngardigal, R.  
674 Smith, C. Chapuis and S. Zentout for technical assistance with the experiments, and Ç. Tuna for help with the  
675 image analysis. This work was supported by the *Centre National de la Recherche Scientifique* (CNRS), the  
676 University of Rennes 1, the *Ligue Contre le Cancer Comité d'Ille et Vilaine et du Finistère* and the *Association*  
677 *pour la Recherche sur le Cancer* (ARC) to G.B., and by the *Institut National du Cancer* (INCa) and *ITMO*  
678 *Cancer/Aviesan* to M.T. E.B.G. was supported by a fellowship from the *Ligue Contre le Cancer* and *Région*  
679 *Bretagne* (Brittany region, France).

## 681 **Author Contributions**

682 E.B.G. designed, performed and analyzed the experiments and wrote the manuscript; A.C. performed the  
683 experiments and revised the manuscript, M.T. co-supervised the work, revised the manuscript and provided  
684 funding; G.B. co-supervised the work, designed the experiments, edited and revised the manuscript, and  
685 provided funding.

## 687 **Conflict of interest**

688 The authors declare no conflict of interest.

## 690 **References**

- 691 1. Ohsumi, Y. Historical Landmarks of Autophagy Research. *Cell Research* **2014**, *24*, 9–23,  
692 doi:10.1038/cr.2013.169.
- 693 2. Klionsky, D.J.; Emr, S.D. Autophagy as a Regulated Pathway of Cellular Degradation. *Science* **2000**,  
694 *290*, 1717–1721, doi:10.1126/science.290.5497.1717.
- 695 3. Deretic, V.; Levine, B. Autophagy, Immunity, and Microbial Adaptations. *Cell Host & Microbe* **2009**,  
696 *5*, 527–549, doi:10.1016/j.chom.2009.05.016.
- 697 4. Rodriguez-Rocha, H.; Garcia-Garcia, A.; Panayiotidis, M.I.; Franco, R. DNA Damage and Autophagy.  
698 *Mutation Research/Fundamental and Molecular Mechanisms of Mutagenesis* **2011**, *711*, 158–166,  
699 doi:10.1016/j.mrfmmm.2011.03.007.
- 700 5. Axe, E.L.; Walker, S.A.; Manifava, M.; Chandra, P.; Roderick, H.L.; Habermann, A.; Griffiths, G.;  
701 Ktistakis, N.T. Autophagosome Formation from Membrane Compartments Enriched in  
702 Phosphatidylinositol 3-Phosphate and Dynamically Connected to the Endoplasmic Reticulum. *J Cell*  
703 *Biol* **2008**, *182*, 685–701, doi:10.1083/jcb.200803137.
- 704 6. Mizushima, N.; Yoshimori, T.; Ohsumi, Y. The Role of Atg Proteins in Autophagosome Formation.  
705 *Annu Rev Cell Dev Biol* **2011**, *27*, 107–132, doi:10.1146/annurev-cellbio-092910-154005.
- 706 7. Ichimura, Y.; Kirisako, T.; Takao, T.; Satomi, Y.; Shimonishi, Y.; Ishihara, N.; Mizushima, N.; Tanida,  
707 I.; Kominami, E.; Ohsumi, M.; et al. A Ubiquitin-like System Mediates Protein Lipidation. *Nature* **2000**,  
708 *408*, 488–492, doi:10.1038/35044114.
- 709 8. Weidberg, H.; Shvets, E.; Shpilka, T.; Shimron, F.; Shinder, V.; Elazar, Z. LC3 and GATE-  
710 16/GABARAP Subfamilies Are Both Essential yet Act Differently in Autophagosome Biogenesis. *The*  
711 *EMBO Journal* **2010**, *29*, 1792–1802, doi:10.1038/emboj.2010.74.
- 712 9. Noda, N.N.; Ohsumi, Y.; Inagaki, F. Atg8-Family Interacting Motif Crucial for Selective Autophagy.  
713 *FEBS Letters* **2010**, *584*, 1379–1385, doi:10.1016/j.febslet.2010.01.018.

- 714 10. Shpilka, T.; Weidberg, H.; Pietrokovski, S.; Elazar, Z. Atg8: An Autophagy-Related Ubiquitin-like  
715 Protein Family. *Genome Biology* **2011**, *12*, 226, doi:10.1186/gb-2011-12-7-226.
- 716 11. Jatana, N.; Ascher, D.B.; Pires, D.E.V.; Gokhale, R.S.; Thukral, L. Human LC3 and GABARAP  
717 Subfamily Members Achieve Functional Specificity via Specific Structural Modulations. *Autophagy*  
718 **2020**, *16*, 239–255, doi:10.1080/15548627.2019.1606636.
- 719 12. Kirisako, T.; Ichimura, Y.; Okada, H.; Kabeya, Y.; Mizushima, N.; Yoshimori, T.; Ohsumi, M.; Takao,  
720 T.; Noda, T.; Ohsumi, Y. The Reversible Modification Regulates the Membrane-Binding State of  
721 Apg8/Aut7 Essential for Autophagy and the Cytoplasm to Vacuole Targeting Pathway. *J Cell Biol* **2000**,  
722 *151*, 263–276, doi:10.1083/jcb.151.2.263.
- 723 13. Tanida, I.; Sou, Y.; Ezaki, J.; Minematsu-Ikeguchi, N.; Ueno, T.; Kominami, E.  
724 HsAtg4B/HsApg4B/Autophagin-1 Cleaves the Carboxyl Termini of Three Human Atg8 Homologues  
725 and Delipidates Microtubule-Associated Protein Light Chain 3- and GABAA Receptor-Associated  
726 Protein-Phospholipid Conjugates. *J Biol Chem* **2004**, *279*, 36268–36276, doi:10.1074/jbc.M401461200.
- 727 14. Kabeya, Y.; Mizushima, N.; Yamamoto, A.; Oshitani-Okamoto, S.; Ohsumi, Y.; Yoshimori, T. LC3,  
728 GABARAP and GATE16 Localize to Autophagosomal Membrane Depending on Form-II Formation.  
729 *Journal of Cell Science* **2004**, *117*, 2805–2812, doi:10.1242/jcs.01131.
- 730 15. Hanada, T.; Noda, N.N.; Satomi, Y.; Ichimura, Y.; Fujioka, Y.; Takao, T.; Inagaki, F.; Ohsumi, Y. The  
731 Atg12-Atg5 Conjugate Has a Novel E3-like Activity for Protein Lipidation in Autophagy. *J Biol Chem*  
732 **2007**, *282*, 37298–37302, doi:10.1074/jbc.C700195200.
- 733 16. Martens, S.; Fracchiolla, D. Activation and Targeting of ATG8 Protein Lipidation. *Cell Discov* **2020**, *6*,  
734 1–11, doi:10.1038/s41421-020-0155-1.
- 735 17. Nakatogawa, H.; Ichimura, Y.; Ohsumi, Y. Atg8, a Ubiquitin-like Protein Required for Autophagosome  
736 Formation, Mediates Membrane Tethering and Hemifusion. *Cell* **2007**, *130*, 165–178,  
737 doi:10.1016/j.cell.2007.05.021.

- 738 18. Xie, Z.; Nair, U.; Klionsky, D.J. Atg8 Controls Phagophore Expansion during Autophagosome  
739 Formation. *Mol Biol Cell* **2008**, *19*, 3290–3298, doi:10.1091/mbc.E07-12-1292.
- 740 19. Pankiv, S.; Clausen, T.H.; Lamark, T.; Brech, A.; Bruun, J.-A.; Outzen, H.; Øvervatn, A.; Bjørkøy, G.;  
741 Johansen, T. P62/SQSTM1 Binds Directly to Atg8/LC3 to Facilitate Degradation of Ubiquitinated  
742 Protein Aggregates by Autophagy. *J Biol Chem* **2007**, *282*, 24131–24145, doi:10.1074/jbc.M702824200.
- 743 20. Mizushima, N. The ATG Conjugation Systems in Autophagy. *Current Opinion in Cell Biology* **2020**,  
744 *63*, 1–10, doi:10.1016/j.ceb.2019.12.001.
- 745 21. Nair, U.; Yen, W.-L.; Mari, M.; Cao, Y.; Xie, Z.; Baba, M.; Reggiori, F.; Klionsky, D.J. A Role for  
746 Atg8–PE Deconjugation in Autophagosome Biogenesis. *Autophagy* **2012**, *8*, 780–793,  
747 doi:10.4161/auto.19385.
- 748 22. Nakatogawa, H.; Ishii, J.; Asai, E.; Ohsumi, Y. Atg4 Recycles Inappropriately Lipidated Atg8 to Promote  
749 Autophagosome Biogenesis. *Autophagy* **2012**, *8*, 177–186, doi:10.4161/auto.8.2.18373.
- 750 23. Yu, Z.-Q.; Ni, T.; Hong, B.; Wang, H.-Y.; Jiang, F.-J.; Zou, S.; Chen, Y.; Zheng, X.-L.; Klionsky, D.J.;  
751 Liang, Y.; et al. Dual Roles of Atg8–PE Deconjugation by Atg4 in Autophagy. *Autophagy* **2012**, *8*, 883–  
752 892, doi:10.4161/auto.19652.
- 753 24. Agrotis, A.; Pengo, N.; Burden, J.J.; Ketteler, R. Redundancy of Human ATG4 Protease Isoforms in  
754 Autophagy and LC3/GABARAP Processing Revealed in Cells. *Autophagy* **2019**, *15*, 976–997,  
755 doi:10.1080/15548627.2019.1569925.
- 756 25. Nguyen, T.N.; Padman, B.S.; Zellner, S.; Khuu, G.; Uoselis, L.; Lam, W.K.; Skulsuppaisarn, M.;  
757 Lindblom, R.S.J.; Watts, E.M.; Behrends, C.; et al. ATG4 Family Proteins Drive Phagophore Growth  
758 Independently of the LC3/GABARAP Lipidation System. *Mol Cell* **2021**, *81*, 2013-2030.e9,  
759 doi:10.1016/j.molcel.2021.03.001.
- 760 26. Betin, V.M.S.; Singleton, B.K.; Parsons, S.F.; Anstee, D.J.; Lane, J.D. Autophagy Facilitates Organelle  
761 Clearance during Differentiation of Human Erythroblasts: Evidence for a Role for ATG4 Paralogs during  
762 Autophagosome Maturation. *Autophagy* **2013**, *9*, 881–893, doi:10.4161/auto.24172.

- 763 27. Levine, B.; Kroemer, G. Biological Functions of Autophagy Genes: A Disease Perspective. *Cell* **2019**,  
764 176, 11–42, doi:10.1016/j.cell.2018.09.048.
- 765 28. Galluzzi, L.; Bravo-San Pedro, J.M.; Levine, B.; Green, D.R.; Kroemer, G. Pharmacological Modulation  
766 of Autophagy: Therapeutic Potential and Persisting Obstacles. *Nature Reviews Drug Discovery* **2017**,  
767 16, 487–511, doi:10.1038/nrd.2017.22.
- 768 29. Ariosa, A.R.; Lahiri, V.; Lei, Y.; Yang, Y.; Yin, Z.; Zhang, Z.; Klionsky, D.J. A Perspective on the Role  
769 of Autophagy in Cancer. *Biochimica et Biophysica Acta (BBA) - Molecular Basis of Disease* **2021**, 1867,  
770 166262, doi:10.1016/j.bbadis.2021.166262.
- 771 30. Agrotis, A.; Ketteler, R. On ATG4B as Drug Target for Treatment of Solid Tumours-The Knowns and  
772 the Unknowns. *Cells* **2019**, 9, E53, doi:10.3390/cells9010053.
- 773 31. *Principles of Fluorescence Spectroscopy*;
- 774 32. Truong, K.; Ikura, M. The Use of FRET Imaging Microscopy to Detect Protein–Protein Interactions and  
775 Protein Conformational Changes in Vivo. *Current Opinion in Structural Biology* **2001**, 11, 573–578,  
776 doi:10.1016/S0959-440X(00)00249-9.
- 777 33. Sizaire, F.; Tramier, M. FRET-Based Biosensors: Genetically Encoded Tools to Track Kinase Activity  
778 in Living Cells. *Protein Phosphorylation* **2017**, doi:10.5772/intechopen.71005.
- 779 34. Padilla-Parra, S.; Tramier, M. FRET Microscopy in the Living Cell: Different Approaches, Strengths  
780 and Weaknesses. *Truong & Ikura* **2012**, 34, 369–376, doi:10.1002/bies.201100086.
- 781 35. Sugawara, K.; Suzuki, N.N.; Fujioka, Y.; Mizushima, N.; Ohsumi, Y.; Inagaki, F. Structural Basis for  
782 the Specificity and Catalysis of Human Atg4B Responsible for Mammalian Autophagy. *J Biol Chem*  
783 **2005**, 280, 40058–40065, doi:10.1074/jbc.M509158200.
- 784 36. Kabeya, Y.; Mizushima, N.; Ueno, T.; Yamamoto, A.; Kirisako, T.; Noda, T.; Kominami, E.; Ohsumi,  
785 Y.; Yoshimori, T. LC3, a Mammalian Homologue of Yeast Apg8p, Is Localized in Autophagosome  
786 Membranes after Processing. *EMBO J* **2000**, 19, 5720–5728, doi:10.1093/emboj/19.21.5720.

- 787 37. Erard, M.; Fredj, A.; Pasquier, H.; Beltolngar, D.-B.; Bousmah, Y.; Derrien, V.; Vincent, P.; Merola, F.  
788 Minimum Set of Mutations Needed to Optimize Cyan Fluorescent Proteins for Live Cell Imaging. *Mol.*  
789 *BioSyst.* **2013**, *9*, 258–267, doi:10.1039/C2MB25303H.
- 790 38. Bertolin, G.; Sizaire, F.; Déméautis, C.; Chapuis, C.; Mérola, F.; Erard, M.; Tramier, M. Optimized  
791 FRET Pairs and Quantification Approaches To Detect the Activation of Aurora Kinase A at Mitosis.  
792 *ACS Sens* **2019**, *4*, 2018–2027, doi:10.1021/acssensors.9b00486.
- 793 39. Bousmah, Y.; Valenta, H.; Bertolin, G.; Singh, U.; Nicolas, V.; Pasquier, H.; Tramier, M.; Merola, F.;  
794 Erard, M. TdLanYFP, a Yellow, Bright, Photostable, and PH-Insensitive Fluorescent Protein for Live-  
795 Cell Imaging and Förster Resonance Energy Transfer-Based Sensing Strategies. *ACS Sens* **2021**, *6*,  
796 3940–3947, doi:10.1021/acssensors.1c00874.
- 797 40. Tanida, I.; Minematsu-Ikeguchi, N.; Ueno, T.; Kominami, E. Lysosomal Turnover, but Not a Cellular  
798 Level, of Endogenous LC3 Is a Marker for Autophagy. *Autophagy* **2005**, *1*, 84–91,  
799 doi:10.4161/auto.1.2.1697.
- 800 41. Nash, Y.; Schmukler, E.; Trudler, D.; Pinkas-Kramarski, R.; Frenkel, D. DJ-1 Deficiency Impairs  
801 Autophagy and Reduces Alpha-Synuclein Phagocytosis by Microglia. *J Neurochem* **2017**, *143*, 584–594,  
802 doi:10.1111/jnc.14222.
- 803 42. Li, M.; Hou, Y.; Wang, J.; Chen, X.; Shao, Z.-M.; Yin, X.-M. Kinetics Comparisons of Mammalian Atg4  
804 Homologues Indicate Selective Preferences toward Diverse Atg8 Substrates. *J Biol Chem* **2011**, *286*,  
805 7327–7338, doi:10.1074/jbc.M110.199059.
- 806 43. Agrotis, A.; von Chamier, L.; Oliver, H.; Kiso, K.; Singh, T.; Ketteler, R. Human ATG4 Autophagy  
807 Proteases Counteract Attachment of Ubiquitin-like LC3/GABARAP Proteins to Other Cellular Proteins.  
808 *Journal of Biological Chemistry* **2019**, *294*, 12610–12621, doi:10.1074/jbc.AC119.009977.
- 809 44. Wang, W.; Chen, Z.; Billiar, T.R.; Stang, M.T.; Gao, W. The Carboxyl-Terminal Amino Acids Render  
810 Pro-Human LC3B Migration Similar to Lipidated LC3B in SDS-PAGE. *PLOS ONE* **2013**, *8*, e74222,  
811 doi:10.1371/journal.pone.0074222.

- 812 45. Li, M. Kinetics Comparisons of Mammalian Atg4 Homologues Indicate Selective Preferences toward  
813 Diverse Atg8 Substrates\*. **2011**, 286, 12.
- 814 46. Fujita, N.; Hayashi-Nishino, M.; Fukumoto, H.; Omori, H.; Yamamoto, A.; Noda, T.; Yoshimori, T. An  
815 Atg4B Mutant Hampers the Lipidation of LC3 Paralogues and Causes Defects in Autophagosome  
816 Closure. *Mol Biol Cell* **2008**, 19, 4651–4659, doi:10.1091/mbc.e08-03-0312.
- 817 47. Skytte Rasmussen, M.; Mouilleron, S.; Kumar Shrestha, B.; Wirth, M.; Lee, R.; Bowitz Larsen, K.;  
818 Abudu Princely, Y.; O'Reilly, N.; Sjøttem, E.; Tooze, S.A.; et al. ATG4B Contains a C-Terminal LIR  
819 Motif Important for Binding and Efficient Cleavage of Mammalian Orthologs of Yeast Atg8. *Autophagy*  
820 **2017**, 13, 834–853, doi:10.1080/15548627.2017.1287651.
- 821 48. Steinhilb, M.L.; Turner, R.S.; Gaut, J.R. The Protease Inhibitor, MG132, Blocks Maturation of the  
822 Amyloid Precursor Protein Swedish Mutant Preventing Cleavage by Beta-Secretase. *J Biol Chem* **2001**,  
823 276, 4476–4484, doi:10.1074/jbc.M008793200.
- 824 49. Harer, S.L.; Bhatia, M.S.; Bhatia, N.M. Proteasome Inhibitors Mechanism; Source for Design of Newer  
825 Therapeutic Agents. *J Antibiot* **2012**, 65, 279–288, doi:10.1038/ja.2011.84.
- 826 50. Liu, P.-F.; Tsai, K.-L.; Hsu, C.-J.; Tsai, W.-L.; Cheng, J.-S.; Chang, H.-W.; Shiao, C.-W.; Goan, Y.-G.;  
827 Tseng, H.-H.; Wu, C.-H.; et al. Drug Repurposing Screening Identifies Tioconazole as an ATG4 Inhibitor  
828 That Suppresses Autophagy and Sensitizes Cancer Cells to Chemotherapy. *Theranostics* **2018**, 8, 830–  
829 845, doi:10.7150/thno.22012.
- 830 51. Bosc, D.; Vezenkov, L.; Bortnik, S.; An, J.; Xu, J.; Choutka, C.; Hannigan, A.M.; Kovacic, S.; Loo, S.;  
831 Clark, P.G.K.; et al. A New Quinoline-Based Chemical Probe Inhibits the Autophagy-Related Cysteine  
832 Protease ATG4B. *Sci Rep* **2018**, 8, 11653, doi:10.1038/s41598-018-29900-x.
- 833 52. Qiu, Z.; Kuhn, B.; Aebi, J.; Lin, X.; Ding, H.; Zhou, Z.; Xu, Z.; Xu, D.; Han, L.; Liu, C.; et al. Discovery  
834 of Fluoromethylketone-Based Peptidomimetics as Covalent ATG4B (Autophagin-1) Inhibitors  
835 Available online: <https://pubs.acs.org/doi/pdf/10.1021/acsmchemlett.6b00208> (accessed on 5 April  
836 2022).

- 837 53. Chu, J.; Fu, Y.; Xu, J.; Zheng, X.; Gu, Q.; Luo, X.; Dai, Q.; Zhang, S.; Liu, P.; Hong, L.; et al. ATG4B  
838 Inhibitor FMK-9a Induces Autophagy Independent on Its Enzyme Inhibition. *Arch Biochem Biophys*  
839 **2018**, *644*, 29–36, doi:10.1016/j.abb.2018.03.001.
- 840 54. Akin, D.; Wang, S.K.; Habibzadegah-Tari, P.; Law, B.; Ostrov, D.; Li, M.; Yin, X.-M.; Kim, J.-S.;  
841 Horenstein, N.; Dunn, W.A. A Novel ATG4B Antagonist Inhibits Autophagy and Has a Negative Impact  
842 on Osteosarcoma Tumors. *Autophagy* **2014**, *10*, 2021–2035, doi:10.4161/auto.32229.
- 843 55. Nguyen, T.G.; Honson, N.S.; Arns, S.; Davis, T.L.; Dhe-Paganon, S.; Kovacic, S.; Kumar, N.S.; Pfeifer,  
844 T.A.; Young, R.N. Development of Fluorescent Substrates and Assays for the Key Autophagy-Related  
845 Cysteine Protease Enzyme, ATG4B. *Assay Drug Dev Technol* **2014**, *12*, 176–189,  
846 doi:10.1089/adt.2013.561.
- 847 56. Kauffman, K.J.; Yu, S.; Jin, J.; Mugo, B.; Nguyen, N.; O'Brien, A.; Nag, S.; Lystad, A.H.; Melia, T.J.  
848 Delipidation of Mammalian Atg8-Family Proteins by Each of the Four ATG4 Proteases. *Autophagy*  
849 **2018**, *14*, 992–1010, doi:10.1080/15548627.2018.1437341.
- 850 57. Klionsky, D.J.; Abdel-Aziz, A.K.; Abdelfatah, S.; Abdellatif, M.; Abdoli, A.; Abel, S.; Abeliovich, H.;  
851 Abildgaard, M.H.; Abudu, Y.P.; Acevedo-Arozena, A.; et al. Guidelines for the Use and Interpretation  
852 of Assays for Monitoring Autophagy (4th Edition). *null* **2021**, 1–382,  
853 doi:10.1080/15548627.2020.1797280.
- 854 58. Li, M.; Chen, X.; Ye, Q.-Z.; Vogt, A.; Yin, X.-M. A High-Throughput FRET-Based Assay for  
855 Determination of Atg4 Activity. *Autophagy* **2012**, *8*, 401–412, doi:10.4161/auto.18777.
- 856 59. Scherz-Shouval, R.; Shvets, E.; Fass, E.; Shorer, H.; Gil, L.; Elazar, Z. Reactive Oxygen Species Are  
857 Essential for Autophagy and Specifically Regulate the Activity of Atg4. *EMBO J* **2007**, *26*, 1749–1760,  
858 doi:10.1038/sj.emboj.7601623.
- 859 60. Nguyen, N.; Olivas, T.J.; Mires, A.; Jin, J.; Yu, S.; Luan, L.; Nag, S.; Kauffman, K.J.; Melia, T.J. The  
860 Insufficiency of ATG4A in Macroautophagy. *Journal of Biological Chemistry* **2020**, *295*, 13584–13600,  
861 doi:10.1074/jbc.RA120.013897.

- 862 61. Xu, D.; Xu, Z.; Han, L.; Liu, C.; Zhou, Z.; Qiu, Z.; Lin, X.; Tang, G.; Shen, H.; Aebi, J.; et al.  
863 Identification of New ATG4B Inhibitors Based on a Novel High-Throughput Screening Platform. *SLAS*  
864 *Discov* **2017**, *22*, 338–347, doi:10.1177/1087057116639202.
- 865 62. Bertolin, G.; Sizaire, F.; Herbomel, G.; Rebutier, D.; Prigent, C.; Tramier, M. A FRET Biosensor  
866 Reveals Spatiotemporal Activation and Functions of Aurora Kinase A in Living Cells. *Nat Commun*  
867 **2016**, *7*, 12674, doi:10.1038/ncomms12674.
- 868 63. Cordelières, F.P.; Zhang, C. 3D Quantitative Colocalisation Analysis. In *Bioimage Data Analysis*  
869 *Workflows*; Miura, K., Sladoje, N., Eds.; Learning Materials in Biosciences; Springer International  
870 Publishing: Cham, 2020; pp. 33–66 ISBN 978-3-030-22386-1.
- 871 64. SMART Available online: <https://smart.servier.com/> (accessed on 3 May 2022).
- 872

# **The LC3B FRET biosensor monitors the modes of action of ATG4B during autophagy in living cells**

**Elif Begüm Gökerküçük et al.**

**Main figures**

## Figure 1

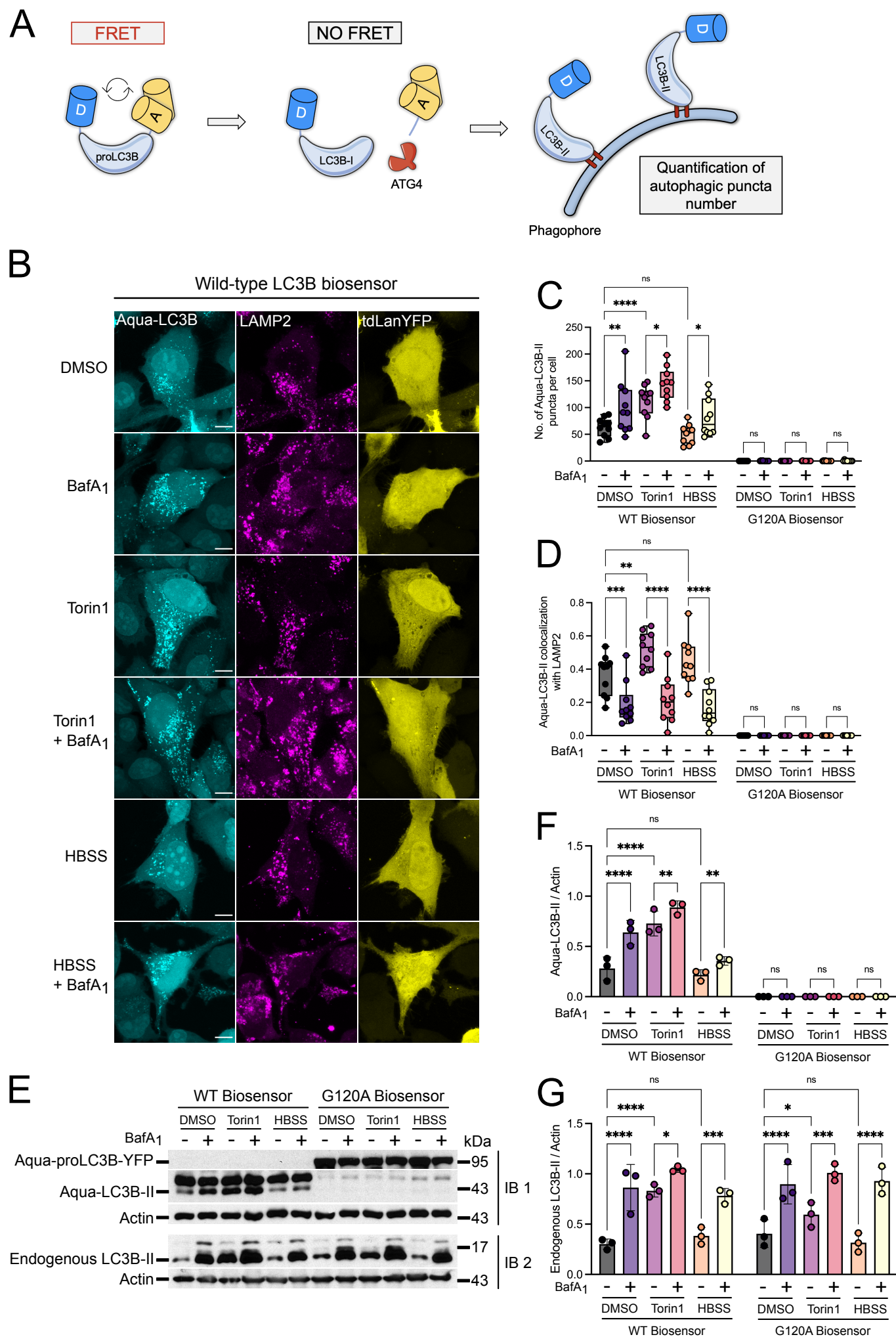


**Figure 1. The LC3B biosensor reports on autophagy induction and/or lysosomal inhibition, and colocalizes with LAMP2 in an autophagy-dependent manner.** (A) The cartoon illustrates the design and the mode of action of the LC3B biosensor. The biosensor was designed to flank the N- and C- termini of proLC3B with a donor (D, Aquamarine)-acceptor (A, tdLanYFP) FRET pair. When ATG4 is not active, the biosensor is expected to remain unprocessed in cells, allowing Aquamarine and tdLanYFP to perform FRET. Upon the proteolytic activity of ATG4, the biosensor is expected to be cleaved at its C-terminus, in turn losing its tdLanYFP moiety and the FRET effect with it. A successful priming of the biosensor is expected to yield Aquamarine-LC3B-I, which can then be integrated into the PE head groups of the phagophores and observed as puncta-shaped structures. The resulting Aquamarine-LC3B-II puncta-shaped structures can then be quantified to estimate the number of autophagosomes. (B) Representative fluorescence images of U2OS cells expressing the WT biosensor and stained for endogenous LAMP2. To investigate the changes in Aqua-LC3B puncta numbers and their colocalization with LAMP2, cells were treated with the following compounds: DMSO (6h), BafA<sub>1</sub> (6h, 100 nM), Torin1 (3h, 250 nM), Torin1 (3h, 250 nM) + BafA<sub>1</sub> (6h, 100 nM), HBSS (1h), HBSS (1h) + BafA<sub>1</sub> (6h, 100 nM). Scale bar: 9 μm. (C) Quantification of the number of Aqua-LC3B-II puncta in cells expressing the WT or G120A biosensor and treated as indicated. (D) Quantification of the ratio of Aqua-LC3B-II puncta structures colocalizing with LAMP2-positive objects in cells expressing the WT or G120A biosensor and treated as indicated.  $n = 10$  cells per condition from one representative experiment (of three) in (C) and (D). (E) Representative western blotting images and corresponding quantifications (F, G) of total lysates from U2OS cells expressing the WT or G120A biosensor and treated as indicated. IB1 and IB2 correspond to the same lysates blotted for overexpressed (IB1) or endogenous (IB2) LC3B forms. Loading control: Actin.  $n = 3$  independent experiments \* $P < 0.05$ , \*\* $P < 0.01$ , \*\*\* $P < 0.001$ , \*\*\*\* $P < 0.0001$ , ns (not significant) as determined by two-way ANOVA with Tukey's multiple comparison test in (C) and (D), and with two-stage step-up method of Benjamini, Krieger and Yekutieli's multiple comparison test to control the false discovery rate in (F) and (G).

## Figure 2

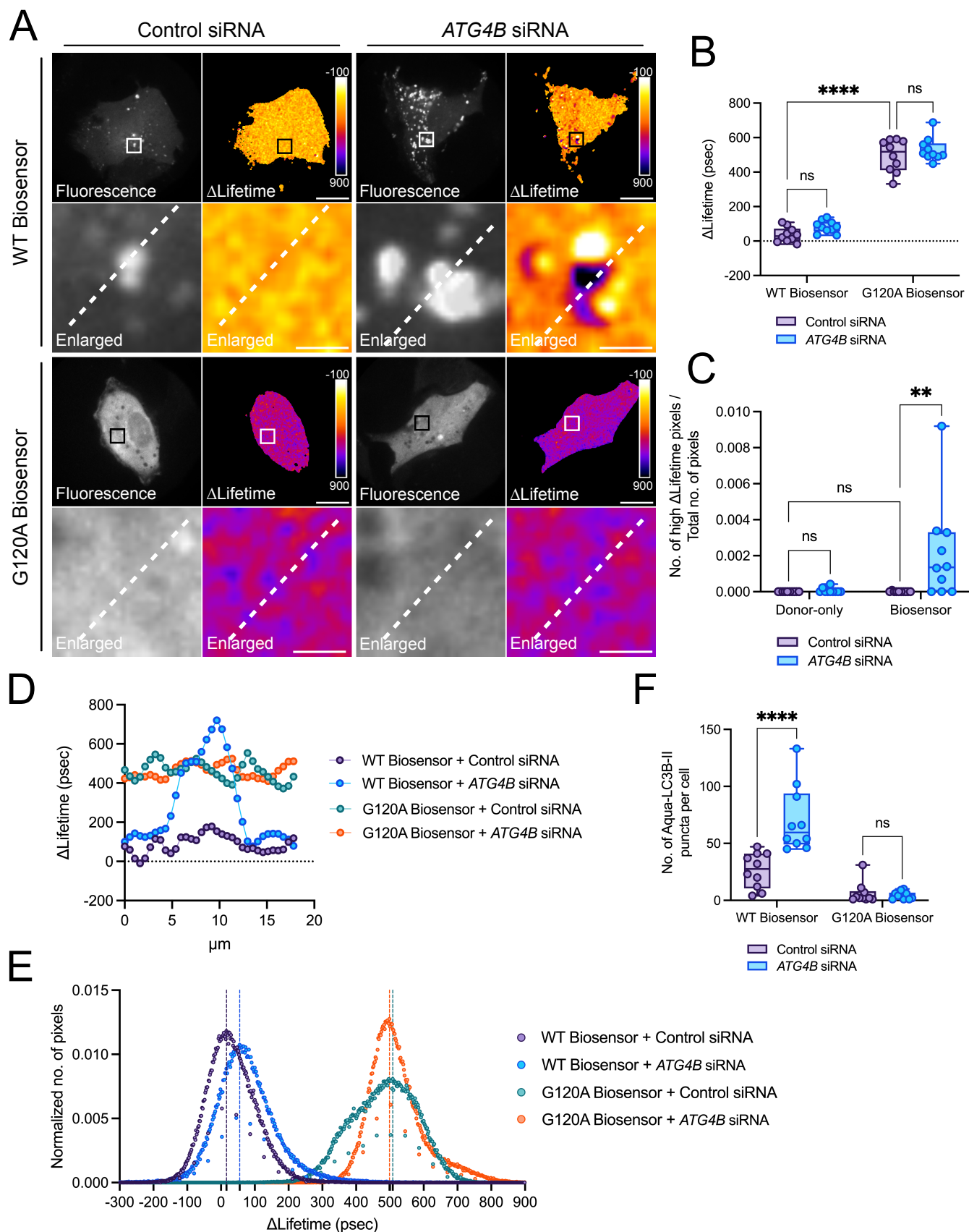
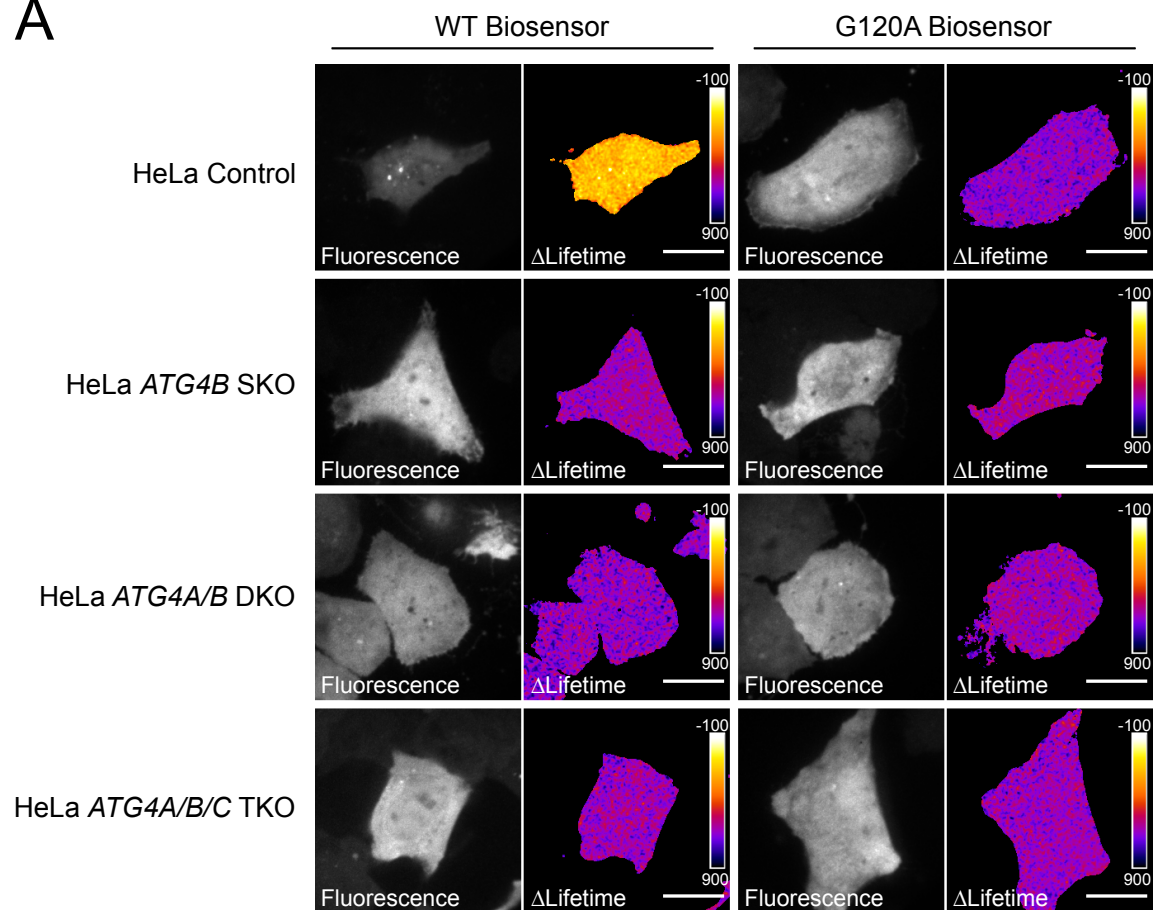


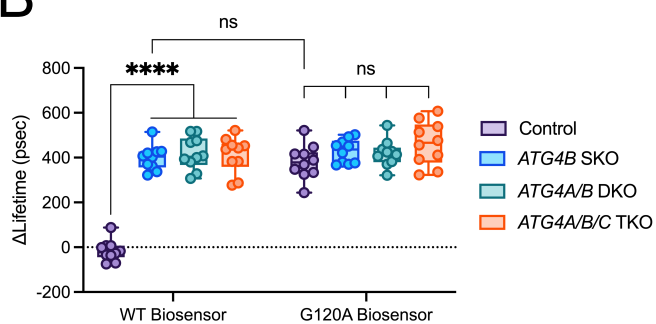
**Figure 2. The knockdown of *ATG4B* lowers the priming of the LC3B biosensor.** (A) Representative fluorescence and  $\Delta$ Lifetime images of U2OS cells co-expressing the WT or G120A biosensor with control or *ATG4B*-specific siRNAs, and analyzed by FRET/FLIM. Squares on the top images of WT or G120A biosensor panels illustrate the location of the enlarged images. Dotted lines on the enlarged images illustrate where the line analysis was performed. Pseudocolor scale: pixel-by-pixel  $\Delta$ Lifetime. Scale bars: overviews, 40  $\mu$ m; enlarged, 6  $\mu$ m. Mean  $\Delta$ Lifetime (B), number of high  $\Delta$ Lifetime pixels (C), line (D), histogram (E), and number of Aqua-LC3B-II puncta (F) analyses of U2OS cells co-expressing the WT or G120A biosensor with control or *ATG4B*-specific siRNAs in (B), (D), (E) and (F), and the WT donor or biosensor with control or *ATG4B* siRNA in (C). Vertical dotted lines on each histogram depicts the mode value in (E).  $n = 10$  cells per condition from one representative experiment (of three) in (B), (C), (E) and (F).  $**P < 0.01$ ,  $****P < 0.0001$ , ns (not significant) as determined by two-way ANOVA with Tukey's multiple comparison test in (B), (C) and (F).

## Figure 3

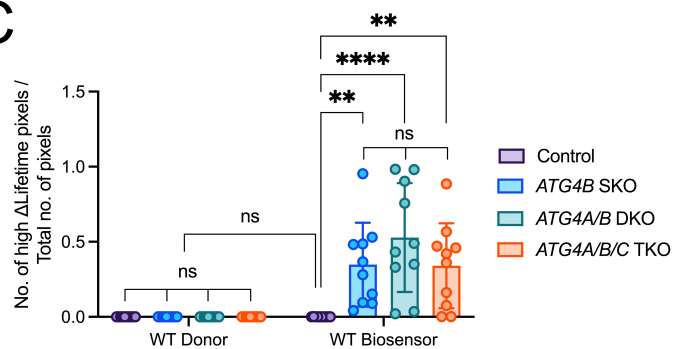
**A**



**B**



**C**



**D**

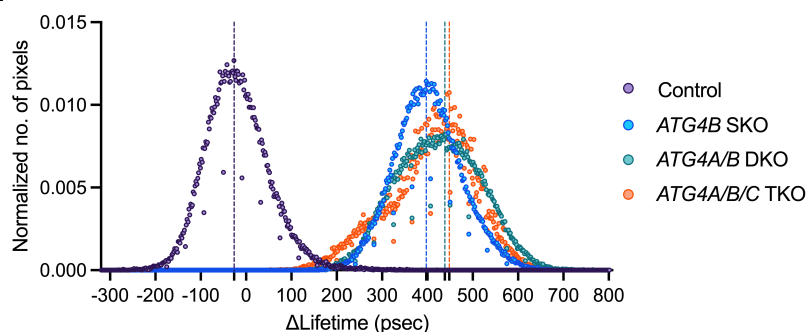


**Figure 3. The absence of ATG4B maximizes the FRET response of the LC3B biosensor.** (A) Representative fluorescence and  $\Delta$ Lifetime images of HeLa control, *ATG4B* SKO, *ATG4A/B* DKO, *ATG4A/B/C* TKO cells expressing the WT or G120A biosensor and analyzed by FRET/FLIM. Pseudocolor scale: pixel-by-pixel  $\Delta$ Lifetime. Scale bar: 40  $\mu$ m. Mean  $\Delta$ Lifetime (B), number of high  $\Delta$ Lifetime pixels (C) and histogram (D) analyses of HeLa control, *ATG4B* SKO, *ATG4A/B* DKO, *ATG4A/B/C* TKO cells expressing the WT or G120A biosensor. The vertical dotted lines on each histogram depict the mode value in (D).  $n = 10$  cells per condition from one representative experiment (of three) in (B), (C) and (D).  $**P < 0.01$ ,  $****P < 0.0001$ , ns (not significant) as determined by two-way ANOVA with Tukey's multiple comparison test in (B) and (C).



**Figure 4. The priming deficiency of the LC3B biosensor is rescued when expressing WT or ATG4B<sup>W142A</sup> in ATG4B SKO cells.** (A) Representative fluorescence and  $\Delta$ Lifetime images of control and ATG4B SKO HeLa cells co-expressing the WT biosensor with an empty vector, or with vectors expressing WT ATG4B, ATG4B<sup>C74S</sup> or ATG4B<sup>W142A</sup>, and analyzed by FRET/FLIM. Pseudocolor scale: pixel-by-pixel  $\Delta$ Lifetime. Scale bar: 40  $\mu$ m. Mean  $\Delta$ Lifetime (B) and number of high  $\Delta$ Lifetime pixels (C) analyses of control and ATG4B SKO cells co-expressing the WT biosensor with an empty vector, or with vectors expressing WT ATG4B, ATG4B<sup>C74S</sup> or ATG4B<sup>W142A</sup>. (D) The histogram analysis of ATG4B SKO cells co-expressing the WT biosensor with an empty vector, or with vectors expressing WT ATG4B, ATG4B<sup>C74S</sup> or ATG4B<sup>W142A</sup>. Vertical dotted lines on each histogram depict the mode value in (D).  $n = 10$  cells per condition from one representative experiment (of three) in (B), (C) and (D). \*\*\*\* $P < 0.0001$ , ns (not significant) as determined by two-way ANOVA with Tukey's multiple comparison test in (B) and (C).

## Figure 5

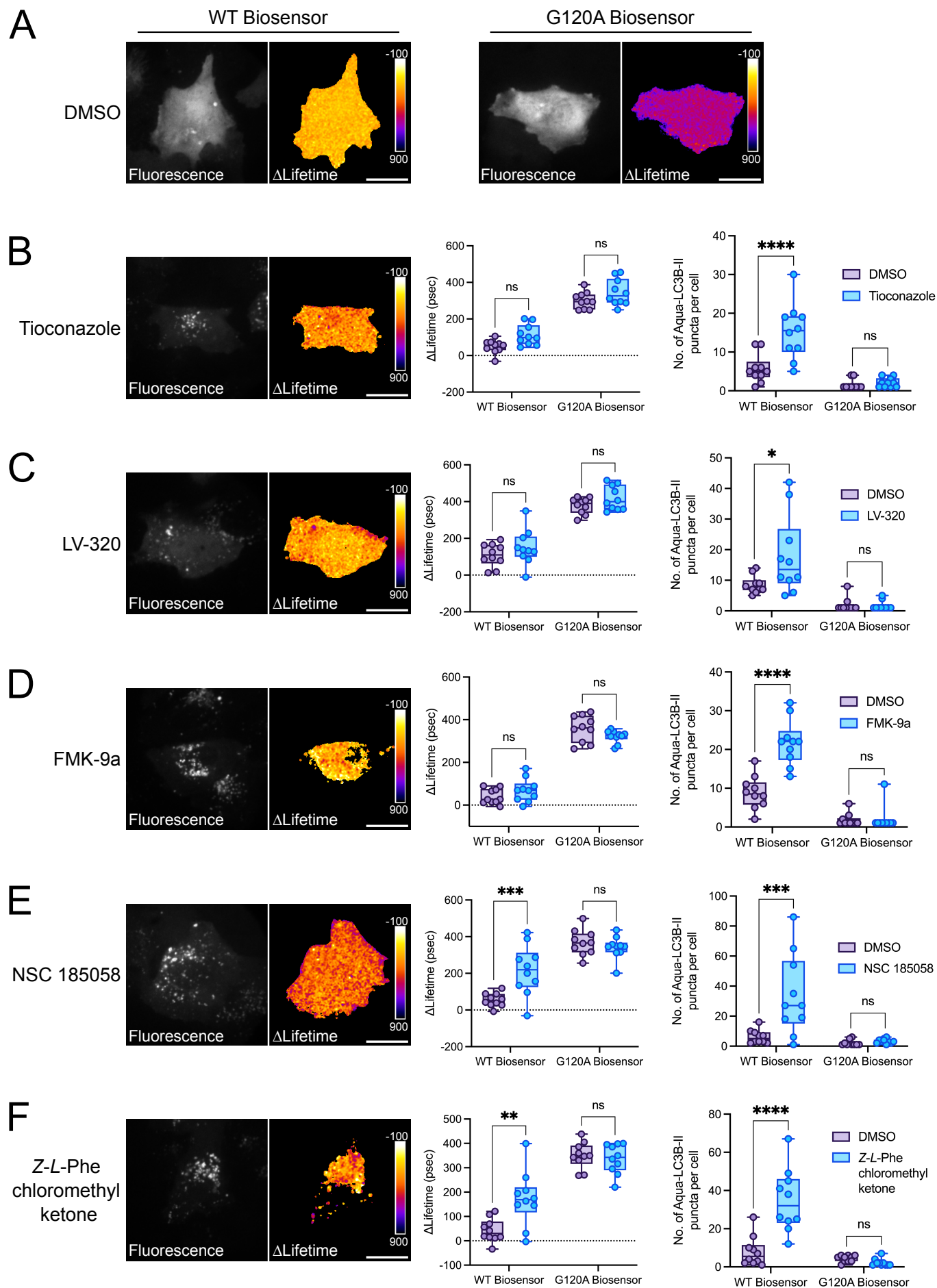


**Figure 5. ATG4B inhibitors variably alter the  $\Delta$ Lifetime behavior and LC3B puncta number in cells expressing the LC3B biosensor.** (A) Representative fluorescence and  $\Delta$ Lifetime images of HeLa cells expressing the WT or G120A biosensor, treated with DMSO (6h), and analyzed by FRET/FLIM. Representative fluorescence and  $\Delta$ Lifetime images of HeLa cells expressing the WT biosensor and treated with Tioconazole (6h, 4  $\mu$ M) (B), LV-320 (6h, 120  $\mu$ M) (C), FMK-9a (6h, 10  $\mu$ M) (D), NSC 185058 (6h, 100  $\mu$ M) (E), or *Z-L*-Phe chloromethyl ketone (6h, 3  $\mu$ M) (F). Mean  $\Delta$ Lifetime and number of Aqua-LC3B-II puncta analyses of HeLa cells expressing the WT or G120A biosensor and treated with Tioconazole (6h, 4 $\mu$ M) (B), LV-320 (6h, 120  $\mu$ M) (C), FMK-9a (6h, 10  $\mu$ M) (D), NSC 185058 (6h, 100  $\mu$ M) (E), or *Z-L*-Phe chloromethyl ketone (6h, 3  $\mu$ M) (F). Pseudocolor scale: pixel-by-pixel  $\Delta$ Lifetime. Scale bars: 40  $\mu$ m.  $n = 10$  cells per condition from one representative experiment (of three) in (B-F). \* $P < 0.05$ , \*\* $P < 0.01$ , \*\*\* $P < 0.001$ , \*\*\*\* $P < 0.0001$ , ns (not significant) as determined by two-way ANOVA with Tukey's multiple comparison test in (B-F).

## Figure 6

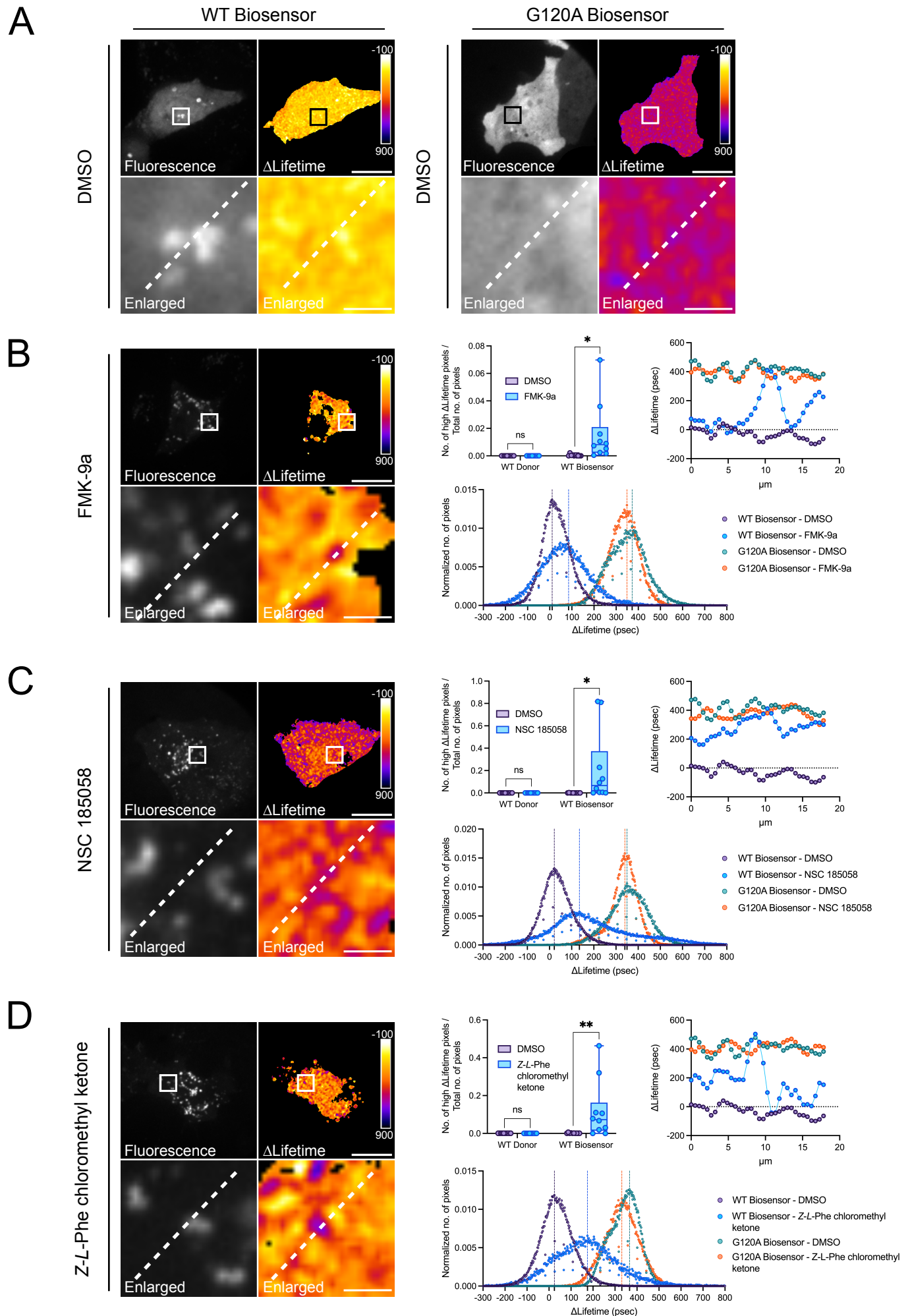


**Figure 6. The LC3B biosensor reveals the mode of action of FMK-9a, NSC 185058 and Z-L-Phe chloromethyl ketone in cells.** (A) Representative fluorescence and  $\Delta$ Lifetime images of HeLa cells expressing the WT or G120A biosensor, treated with DMSO (6h), and analyzed by FRET/FLIM. Representative fluorescence and  $\Delta$ Lifetime images of HeLa cells expressing the WT biosensor and treated with the following compounds: FMK-9a (6h, 10  $\mu$ M) (B), NSC 185058 (6h, 100  $\mu$ M) (C), or Z-L-Phe chloromethyl ketone (6h, 3  $\mu$ M) (D). Squares on the top images of WT or G120A biosensor panels illustrate the location of the enlarged images. Dotted lines on the enlarged images illustrate where the line analysis was performed. Pseudocolor scale: pixel-by-pixel  $\Delta$ Lifetime. Scale bars: overviews, 40  $\mu$ m; enlarged, 6  $\mu$ m. Number of high  $\Delta$ Lifetime pixels analysis of HeLa cells expressing the WT donor or biosensor and treated with FMK-9a (6h, 10  $\mu$ M) (B), NSC 185058 (6h, 100  $\mu$ M) (C), or Z-L-Phe chloromethyl ketone (6h, 3  $\mu$ M) (D). Line and histogram analyses of HeLa cells expressing the WT or G120A biosensor and treated with FMK-9a (6h, 10  $\mu$ M) (B), NSC 185058 (6h, 100  $\mu$ M) (C), or Z-L-Phe chloromethyl ketone (6h, 3  $\mu$ M) (D).  $n = 10$  cells per condition from one representative experiment (of three) in (B-D). \* $P < 0.05$ , \*\* $P < 0.01$ , ns (not significant) as determined by two-way ANOVA with Tukey's multiple comparison test in (B-D).